ELM suppression in helium plasmas with 3D magnetic fields

T. E. Evans[1], A. Loarte[2], D. M. Orlov[3], B. A. Grierson[4], M. M. Knölker [5], B. C. Lyons[1,6], L. Cui[4], P. Gohil[1], R. J. Groebner[1], R. A. Moyer[3], R. Nazikian[4], T. H. Osborne[1] and E. A. Unterberg[7]

[1]General Atomics, P.O. Box 85608, San Diego, California 92186-5608, USA
[2]ITER Organization, Route de Vinon sur Verdon, 13067 St Paul lez Durance, France
[3]University of California San Diego, La Jolla, California 92093, USA
[4]Princeton Plasma Physics Laboratory, PO Box 451, Princeton, New Jersey 08543-0451, USA
[5]Ludwigs Maximilians Universitaet, München, Germany
[6]Oak Ridge Institute for Science Education, Oak Ridge, Tennessee 37831-8072, USA
[7]Oak Ridge National Laboratory, Oak Ridge, Tennessee 37831-8072, USA

E-mail contact of main author: evans@fusion.gat.com

Abstract

Experiments in DIII-D, using non-axisymmetric magnetic perturbation fields in high-purity low toroidal rotation, ^{4}He plasmas have resulted in Type-I Edge Localized Mode (ELM) suppression and mitigation. Suppression is obtained in plasmas with zero net input torque near the L-H power threshold using either Electron Cyclotron Resonant Heating (ECRH) or balanced co- and counter-I_p Neutral Beam Injection (NBI) resulting in conditions equivalent to those expected in ITER's non-active operating phase. In low-power ECRH H-modes, periods with uncontrolled density and impurity radiation excursions are prevented by applying n=3 non-axisymmetric magnetic perturbation fields. ELM suppression results from a reduction and an outward shift of the electron pressure gradient peak compared to that in the high-power ELMing phase. The change in the electron pressure gradient peak is primarily due to a drop in the pedestal temperature rather than the pedestal density.

1. Introduction

The success of the ITER experiment, an essential stepping-stone for developing magnetically confined burning fusion plasma power reactors, relies on our ability to understand the physics required to control MHD instabilities known as Edge-Localized Modes (ELMs). Large ELM instabilities in burning ITER plasmas are expected to release peak thermal energies approaching 20-30 MJ, along with high velocity ionized particles, in several hundred microseconds. This poses a challenge to the lifetime of the plasma facing components due to the ELM-driven transient erosion. In addition, the impurity influxes caused by this large transient erosion have the potential to trigger plasma

disruptions that can result in large thermal loads onto the plasma facing components as well as in large mechanical loads on the in-vessel components and the vacuum vessel itself, if they are not mitigated.

A promising approach for reducing the severity of these ELMs, referred to as mitigation, or completely suppressing the instability is based on using non-axisymmetric magnetic perturbation fields consisting of resonant (RMP) and non-resonant (NRMP) spectral components [1][2]. These fields are applied with specialized non-axisymmetric coils located either inside [2][3][4][5][6] or outside the vacuum vessel [7][8]. An important milestone for the ITER project, during its initial non-active operational phase, in which ^{1}H and ^{4}He plasmas will be explored, is to demonstrate that large type-I ELMs can be sufficiently well controlled using either small non-axisymmetric magnetic fields and/or cryogenic hydrogen (^{1}H) pellet pacing [9][10][11]. Achieving this milestone decreases the risk in carrying out ITER's goal of Q =10 in deuterium-tritium (^{2}H-^{3}H) plasmas in the nuclear phase, for which H-mode confinement and ELM control is required, as it allows demonstration and optimization of the required techniques well in advance of its application during nuclear operations..

In ITER, ELM control requires either the complete elimination of the type-I ELMs, referred to as suppression, or a reduction in the energy of the ELMs striking the plasmas facing components to less than the divertor material erosion threshold; this is typically a reduction of 30-60 with respect to the highest possible uncontrolled ELM loads, referred to as mitigation. Consequently, the ITER research plan [12] relies on achieving H-modes, along with the characterization and development of reliable ELM control techniques, in helium (^{4}He) and/or hydrogen (^{1}H) plasmas during the initial non-active phase of operations where the plasma current (I_p) and toroidal magnetic field (B_T) will be typically limited to $I_p \sim 7.5$ MA and $B_T \sim 2.65$ T due to the L-H power threshold ($P_{L\text{-}H}$) scaling with the isotopic mass and the available heating power [10]. The characteristics of the H-mode performance obtained in the non-active operational phase of ITER will rely on the available level of neutral beam injection heating power (P_{NBI}) along with the electron and ion cyclotron resonance heating power (P_{ECRH} and P_{ICRH}) in combination with the level of Ohmic heating power (P_{OH}) and the choice of main ion plasmas species *i.e.,* ^{1}H or ^{4}He. While it is expected that a sufficient level of additional and Ohmic heating power P_{TOT} =

P_{NBI} + P_{ECRH} + P_{ICRH} + P_{OH} will be available to access H-modes in both ^{1}H and ^{4}He plasmas, it is most likely that the characterization of H-modes and the development of ELM control schemes during the non-active phase of operations will be done in ^{4}He. This is due both to the lower power required to access and sustain the H-mode in ^{4}He plasmas compared to ^{1}H and because of the availability of robust ICRH heating schemes for ^{4}He plasmas at 2.65 T which are not available for ^{1}H. This increases the maximum additional heating power for ^{4}He plasmas to 73 MW (33 MW using ^{1}H neutral beam injection heating power (^{1}H-P_{NBI}) and 20 MW of ECRH as well as 20 MW of ICRH), compared to 53 MW for ^{1}H plasmas. Thus, these early ITER H-modes are expected to operate marginally above the $P_{L\text{-}H}$ level with a relatively low level of the toroidal flow velocity (v_ϕ) compared to typical H-mode rotation profiles in existing tokamaks such as DIII-D. These are particularly challenging conditions to duplicate in DIII-D while maintaining core ^{4}He concentrations equal to or greater than 80% but, as described below, after a series of attempts, a DIII-D discharge scenario was developed that matches the ITER ^{4}He non-active operational phase quite well.

In order to better understand the requirements for H-mode operations and reliable ELM control in ^{4}He plasmas during the ITER non-active phase, several experiments have been carried out in DIII-D over the last few years to obtain conditions similar to those expected in ITER. The primary goal of these experiments was to quantify the $P_{L\text{-}H}$ and to develop ELM control techniques in plasmas with low toroidal rotation, high-purity ^{4}He core concentrations (≥ 80%) and P_{TOT} slightly above $P_{L\text{-}H}$. Prior to the most recent ELM mitigation and suppression experiments, attempts were made to suppress ELMs in high-purity ^{4}He plasmas using both ^{4}He neutral beam injection heating power (^{4}He P_{NBI}) and ^{1}H P_{NBI} [13]. These experiments suffered from various technical issues leading, in some cases, to uncontrolled density increases. In order to circumvent these issues, an experiment was done following a fresh boronization of the vacuum vessel walls with a ^{4}He carrier gas and ^{2}H neutral beam injection (^{2}H P_{NBI}) heating, referred to below simply as P_{NBI} heating, that resulted in isolated periods of ELM suppression in discharges with relatively low ^{2}H concentrations [14]. Experience gained from these early attempts resulted in the development of an operating scenario with stable, high-purity, ^{4}He plasmas and H-mode conditions similar to those expected in ITER's non-active ^{4}He

plasmas.

Section 2 describes the operating scenario that was developed to obtain stable high-purity ^{4}He discharges, along with the assessment of the $P_{L\text{-}H}$ in ECRH ^{4}He plasmas. Section 3 provides details on ELM suppression in low toroidal rotation ECRH ^{4}He plasmas and section 4 covers resistive two-fluid modeling of the experimental results discussed in section 3. Section 5 provides a summary of experiments in which ELM suppression was observed at low toroidal rotation using balanced co- and counter-P_{NBI} heated plasmas and section 6 provides an overview of the ELMing behavior observed in low toroidal rotation balanced co- and counter-P_{NBI} heated plasmas during discharges without ELM suppression. The final section provides a discussion and a summary of the key results.

2. Experimental conditions and assessment of L-H power threshold in helium plasmas

In order to make contact with previous DIII-D ELM suppression experiments done in ^{2}H plasmas, these ^{4}He plasmas were operated with I_p = 1.53 MA, B_t = 2.0 T and q_{95} = 3.55 using a plasma shape similar to that planned for ITER Q_{DT} = 10 H-mode operations but scaled down to fit in the DIII-D vacuum vessel. In these discharges, the lower triangularity was increased slightly to δ_L = 0.67, compared to that in the ITER with δ_L = 0.60, for optimal divertor cryopump alignment as shown in figure 1. This configuration is referred to as the ITER Similar Shape (ISS) in DIII-D and has been used extensively in low-collisionality ^{2}H plasma ELM suppression experiments [15].

In these ISS plasmas, with q_{95} = 3.55, the vacuum RMP field spectrum is optimized for producing large resonant magnetic islands at the top of the pedestal plasma and a wide region of stochastic field lines, referred to as the Vacuum Island Overlap Width (VIOW), covering as much as 20% of the outer plasma flux surfaces. In this case, the non-axisymmetric magnetic perturbation fields from the DIII-D I-coil [16] are simply referred to as RMP fields in order to emphasize the resonant aspect of the applied fields. Figure 1 shows the positions of the upper and lower RMP coils, referred to as I-coils, located symmetrically above and below the equatorial plane on the low-field side inside the DIII-D vacuum vessel behind graphite protection tiles. The poloidal positions of the

2nd harmonic ECRH deposition points, above the equatorial plane near the 0.7 normalized poloidal flux (ψ_N) surface, and the radial locations of the ECE diagnostic channels near the equatorial plane are also shown. The ECE channels, starting from channel 1 located in the low-field side scrape-off layer (SOL), through channel 40 located on the high-field side at the ψ_N = 0.2 surface are used to monitor fast electron temperature (T_e) changes. The SOL flux contour lines shown just outside the separatrix are separated at 1 cm intervals on the low-field side equatorial plane. The locations of filterscope channels fs01-04, viewing the lower divertor strike points and private flux region, are also shown in figure 1.

The first step in this experiment was to determine $P_{L\text{-}H}$ using only ECRH. Here, it was found that $P_{L\text{-}H}$ = 2.9 MW and that at this power level the plasma experienced a series of uncontrolled density and core impurity increases followed by back transitions from the H-mode to an L-mode. To prevent this uncontrolled L-H-L behavior in the beginning of the discharge, an operating scenario was developed with an early high-power ^{2}H-NBI and ECRH phase. This high-power phase was then followed by a low-power, low toroidal rotation phase, matching ITER's non-active ^{4}He plasma conditions. In these discharges, 11 Torr-liters of ^{4}He was injected during the first 1100 ms and at 1200 ms, approximately 100 ms after reaching the I_p plateau, the P_{NBI} was increased from 3.7 MW to 8.4 MW resulting in the addition of 36 Torr-liters of ^{2}H fueling over the 2600 ms duration of the ^{2}H-NBI heating phase as determined from global particle balance calculations [17]. In addition, at 1100 ms ECRH was added with P_{ECRH} = 2.9 MW resulting in P_{TOT} = 11.6 MW, including P_{OH} = 0.3 MW. The early high-power, high torque, phase was found to be effective for establishing high toroidal rotation H-mode discharges, which allowed a transition to a low-power phase later in the discharge with ITER similar rotation profiles. An example of this operating scenario is shown in figure 2. Here, the low-power phase started at 3000 ms and had a constant P_{ECRH} = 2.9 MW resulting in $P_{TOT} = P_{ECRH} + P_{OH}$ = 3.7 MW with $v_\phi \cong 0$. Over the course of the experiment, this low-power low-torque H-mode phase was maintained using either ECRH, with a maximum input power of 3.0 MW, or with modulated ^{2}H-NBI heating pulses consisting of short periods with co- plus counter-I_p injection resulting in zero net input torque and P_{NBI} = 1.7 MW. These low-power ^{2}H-NBI phases had P_{OH} = 1.2 MW, resulting in P_{TOT} = 2.9 MW and $v_\phi \cong 0$.

Discharges with the low-power ECRH phase also had short diagnostic ^{2}H-NBI pulses as shown in figure 2b.

In order to minimize the core ^{2}H concentration due to ^{2}H-NBI heating, the DIII-D cryopumps were operated at liquid helium temperatures without an argon frost to enable ^{2}H pumping. It was found that the initial high ^{2}H-NBI heating phase was helpful for releasing neutral ^{2}H from the graphite divertor tiles and exhausting it with the cryopumps. This resulted in a reduction of the ^{2}H core concentration to approximately 40%, which is higher than the acceptable 20% level for the ITER ELM suppression tests during this phase of the discharge. The resulting H-mode line average and pedestal density, as well as the lower divertor D_α (656 nm) signal, using this mode of operation are shown in figure 2a. In addition to the lower divertor D_α filterscope signals, the lower divertor HeII (469 nm), D_β(486 nm), CII (541 nm) and CIII (465 nm) were monitored and found to be similar in amplitude to that of the D_α. Note that in this discharge the RMP field is only applied during the first half of the high-power phase as shown in figure 2b. During this time the line averaged and pedestal densities slowly decay and promptly recover when the RMP field is turned off. This behavior is similar to that seen in ^{2}H discharges during the application of the RMP field although the reduction in the density is somewhat smaller than that seen in similar ^{2}H discharge. Comparing the D_α signals during the application of the RMP field and afterwards, we see that there is an increase in the ELM frequency and a reduction in the ELM amplitude consistent with RMP ELM mitigation seen in ^{2}H plasmas. As seen in figure 2a, following the high-power ^{2}H-NBI heating phase the discharge undergoes a series of uncontrolled ELM-free cycles. During this phase $P_{TOT} = P_{ECRH} + P_{OH} = 3.7$ MW. Figures 2ac show the correlation between these uncontrolled ELM-free phases and substantial increases in the FeXXIII (133 nm) line radiation, which is the dominant core impurity line observed during these cycles. Each of these uncontrolled density and core radiation excursions are terminated by large ELMs with a maximum energy of $\Delta W_{ELM} = 84.7$ kJ, where ΔW_{ELM} is the measured change in the stored plasma energy (W_{MHD}) using a fast diamagnetic loop signal. In addition, the increase in FeXXIII radiation corresponds to an increase in the total core radiated power ($P_{rad\text{-}core}$) from 0.7 MW to 3.0 MW, where $P_{rad\text{-}core} \cong P_{L\text{-}H}$, and $P_{TOT} = 3.7$ MW. In the high-power phase, with $P_{TOT} = 11.6$ MW, $P_{rad\text{-}core} = 3.6$ MW during the time the RMP

field is applied and increases to 4.9 MW without the RMP field suggesting that the 3D field increases the impurity transport during the ELM mitigated phase.

Here, it has been found that ^{4}He discharges, operating just above the H-mode power threshold, experience uncontrolled density and impurity excursions that result in an H to L back transition when the core radiated power reaches the ECRH input power level of 3.0 MW. After dropping back into an L-mode regime, the H-mode transport barrier recovers and the uncontrolled accumulation of core particles repeats resulting in multiple L-H-L cycles during a single discharge as seen in figure 2. Large individual ELMs are randomly triggered during each cycle and multiple ELM bursts are observed just before each H-L back transition. It is not known if these ELM bursts are involved in the rapid loss of confinement leading to the collapse of the H-mode transport barrier.

3. ELM suppression in ECRH helium discharges with low toroidal rotation

As seen in figure 3, by extending the duration of the RMP field into the low-power phase of the discharge, the line average density drops slightly and the ELM frequency is reduced from 56 Hz to 27 Hz following a 200 ms transition period (figure 3a). The low-power ELMing phase is consistent with a reduction in heating power as the discharge drops toward $P_{L\text{-}H}$. In this low-power ^{4}He plasma the ELMs have an average ELM energy loss (ΔW_{ELM}) of approximately 29 kJ, which is similar to the average $\Delta W_{ELM} \cong 31$ kJ in the high-power ELMing phase. This behavior is quite different than ELM mitigation in ^{2}H plasmas where the ELM frequency increases and ΔW_{ELM} is typically reduced by about a factor of 3 when the RMP field is applied and ELM suppression is not obtained. This difference may be a consequence of operating slightly above $P_{L\text{-}H}$ in the ^{4}He discharges. It is also noted that during the transition from the high-power to the low-power phase the stored energy (W_{MHD}) drops from 1.2 MJ to 0.3 MJ and β_N drops from 2.0 to 0.6. Following the low-frequency ELMing phase, there is 300 ms period of ELM suppression starting at 3550 ms as seen in figure 3a. Subsequently, ELM suppression is lost at 3850 ms due to a plasma shape change and a locked mode. Note that the ELM suppression phase at the end of this discharge differs from the ELM-free cycles seen in figure 2ac since the line averaged density, the pedestal density and the FeXXIII (133 nm) line radiation do not undergo an uncontrolled increase. An important consequence of

extending the RMP field into the low-power phase is the elimination of the uncontrolled density accumulations cycles seen in figure 2a and the elimination of the uncontrolled increase in the FeXXIII (133 nm) line radiation during these cycles. Compared to the discharge shown in figure 2, $P_{rad\text{-}core}$ is held to less than 3.7 MW in the high-power phase and 0.8 MW in the low-power ELMing phase with an additional reduction to 0.7 MW in the ELM suppressed phase. The increasing FeXXIII line radiation seen at the end of the high-power phase in figure 3c is accompanied by a factor of 3.2 increase in line radiation from NiXXIII (165 nm) and a factor of 2.2 increase in OVIII (102 nm) indicating the release of impurities from plasma facing surfaces that were not present in the previous discharge shown in figure 2. This is believed to be a consequence of the ^{2}H-NBI heating and the loss of energetic beam ions on exposed metallic surface due to the RMP field [18].

As seen in figure 4a, the low-power ELMing (t = 3500 ms) and ELM suppressed (t = 3800 ms) phases of discharge 158473, have an electron pedestal density (n_e) that is reduced slightly compared to the high-power ELMing phase (t = 2555 ms). The initial reduction in the n_e during the low-power ELMing phase is correlated with a loss in ^{2}H fueling from the ^{2}H-NBI heating and a drop in the D_α baseline by about a factor of 5 starting at 3000 ms. The n_e reduction seen in the suppressed phase (figure 4a at t = 3800 ms) is due to a slow decay of n_e starting at t = 3450, toward the end of the mitigated phase as seen in figure 3a. There is also a large drop of the electron pedestal temperature T_e (figure 4b) following the transition from the high-power to the low-power phase, which is the dominant factor controlling the height and position of the electron pedestal pressure gradient. As seen in figure 4c, the electron pedestal pressure (p_e) drops from 5.5 kPa in the high-power phase to 2.1 kPa in the low-power phase. Additionally, figure 4d shows a significant reduction in the peak p_e gradient along with an outward shift from ψ_N = 0.97 to 0.98. Although the changes in p_e during ELM suppression in ^{4}He discharges are similar to those in ^{2}H ELM suppressed cases the mechanisms involved are different. In ^{2}H discharges the reduction in p_e is caused by a reduction in the n_e which typically leaves T_e unchanged or slightly increased [1]. Although there is some uncertainty in the cause of the transition from ELMing to ELM suppression in the low-power phase, due to the lack of rotation and E_r data, it may be related to the small inward shift of the electron pressure

profile between 3500 ms and 3800 ms.

Extended periods of ELM suppression are also obtained in the low-power phase of similar discharges using only ECRH and infrequent ^{2}H-NBI diagnostic pulses, needed to obtain kinetic plasma profile data with the DIII-D charge exchange recombination diagnostic. As seen in figure 5 during discharge 158434, the line average electron density stabilizes at 4.9×10^{19} m^{-3} ($n_e/n_{GW} = 0.35$) during the high-power H-mode with $P_{NBI} = 9$ MW, $P_{ECRH} = 2.9$ MW and $P_{OH} = 0.9$ MW resulting in $\beta_N = 1.9$. The H_{98Y2} confinement factor is 0.86 during the high-power phase and drops to 0.6 during the low-power ECRH H-mode phase between 3.1 and 4.9 s. Here, the electron pedestal collisionality, defined as [19]:

$$\nu_e^* = 6.921\times10^{-18} q R n_e Z_{eff} ln\Lambda_e T_e^{-2} \varepsilon^{-1/2}, \quad (1)$$

is shown in Table 1 using measurement from visible bremsstrahlung ($\nu_e^{*,brems}$) as well as simulation from the TRANSP code [20] ($\nu_e^{*,transp}$) and spectroscopic data.

	High-Power Phase, 2800 ms $P_{NBI} + P_{ECRH} + P_{OH}$	Low-Power Phase, 4750 ms $P_{ECRH} + P_{OH}$
$\nu_e^{*,brems}$	0.29	1.05
Z_{eff}^{brems}	1.9	2.2
$\nu_e^{*,transp}$	0.42	1.26
Z_{eff}^{transp}	2.65-2.75	2.45-2.65

Table 1 Variations in the electron pedestal collisionality calculated from eq. (1) using an experimentally measured Z_{eff} from bremsstrahlung data and a simulated Z_{eff} from the TRANSP code in discharge 158434 during the high-power and low-power phases.

The increase in ν_e^* between the high-power and low-power phase is dominated by the drop in T_e from 0.92 keV to 0.52 keV with a 16% increase in Z_{eff}^{brems} contributing to a factor of 2.6 increase in $\nu_e^{*,brems}$ while a small drop in Z_{eff}^{transp} results in a smaller factor of 2 increase in $\nu_e^{*,transp}$. As discussed below, the TRANSP analysis also confirms a ^{2}H concentration of approximately 2% in the low-power phase between ^{2}H-NBI diagnostic

pulses. The uncertainty in ν_e^*, resulting from the difference between Z_{eff}^{brems} and Z_{eff}^{transp}, is particularly important during the high-power phase of the discharge because low collisionality ELM suppression in ^{2}H discharges is lost when $\nu_e^* > 0.35$ [21] and high collisionality ELM suppression in ^{2}H plasma is observed when $\nu_e^* > 0.90$ [22][23]. Thus, the lack of ELM suppression in the high-power phase may be due the increased collisionality in these ^{4}He plasmas while suppression in the ECRH phase is consistent with the high-collisionality branch of ELM suppression seen in ^{2}H plasmas. In figure 5a, during the ELM suppressed phase, the line average density drops by about 14% to 4.2 × 10^{19} m^{-3} (n_e/n_{GW} = 0.32), due to the loss of ^{2}H-NBI fueling. The reduction in the pedestal v_ϕ following the high-power phase and the n = 3 RMP coil current is shown in figure 5c.

TRANSP [20] modeling during the high-power phase of discharge 158434 (figure 5) at 2880 ms yielded a ^{4}He density of 1.30 × 10^{19} m^{-3} and a ^{2}H density of 0.77 × 10^{19} m^{-3} or approximately 63% ^{4}He which is lower than the desired value of 80% needed to match the expected ^{4}He core concentration in ITER. In the low-power ECRH phase of 158434 at 4620 ms, between the ^{2}H-NBI diagnostic pulses, the ^{4}He purity improved dramatically to 98% based on the TRANSP modeling result. Here, the ^{4}He density was 1.53 × 10^{19} m^{-3} with a ^{2}H density of 0.03 × 10^{19} m^{-3}. These values are consistent with the measured drop in the neutron flux from 1.15 × 10^{13} neutrons/s in the high-power phase to approximately zero between ^{2}H-NBI pulses and increasing transiently to 1.59 × 10^{11} neutrons/s during the ^{2}H-NBI pulses in the low-power phase. These ion densities are also in reasonable agreement with the measured line average electron densities based on the calculated TRANSP effective charge of Z_{eff}^{transp} = 2.65-2.75 at t = 2880 ms and Z_{eff}^{transp} = 2.45-2.65 at t = 4750 ms.

The primary motivation for undertaking these experiments was to obtain ELM suppression in discharges with low or zero ^{2}H-NBI and ECRH torque in order to match the v_ϕ profiles expected during non-active ^{4}He operations in ITER. Figures 6a and 6b show changes in the toroidal rotation frequency profile (Ω_ϕ) between the high-power ELMing phase of the discharge at 2800 ms and the ELM suppressed phase at 4750 ms. This data confirms that the edge toroidal rotation frequency is strongly reduced from Ω_ϕ

= 25 krad/s at ψ_N = 0.8 to approximately 5 krad/s while the edge rotation near the top of the pedestal increases slightly during the ELM suppressed phase with ECRH. At the same time, the inner part of radial electric field profile (E_r) is reduced and the inner zero crossing of the edge E_r well shifts outward toward the separatrix from ψ_N = 0.93 to ψ_N = 0.97 while the depth of the E_r well across the pedestal is reduced slightly. Although the quality of the core E_r data is rather poor in the low-power phase due to limitations on the ^{2}H-NBI sources required to maintain low torque, the structure of the E_r well in the ELM suppressed phase is typical of that in an ELM suppressed H-mode with an edge transport barrier. In addition, the edge n_e and T_e profiles retain a weak H-mode pedestal structure, similar to that shown in figures 4ab during a companion discharge, although the H-factor and β_N are significantly reduced compared the high-power phase and those typical H-modes in ^{2}H plasmas.

Here, it is shown that ELM suppression is achieved in the low-power H-mode phase of these ^{4}He discharges following a reduction in the pedestal T_e, from the high-power phase resulting from a reduction in the input heating power as shown in figure 4b, when the pedestal electron density and temperature profiles undergo a small radial inward shift as seen in figures 4bc. While the pedestal density drops slightly during ELM suppression it remains slightly above the level typically found during ELM suppression in ^{2}H plasmas. An additional benefit of the RMP field is that it suppresses the uncontrolled accumulation of core particles and the increase in radiated power observed when operating just above the L-H power threshold in these high-purity ^{4}He plasmas.

4. Resistive two-fluid MHD modeling of ECRH ELM suppression

Linear resistive two-fluid MHD modeling of the ELM suppressed ^{4}He plasma discussed in the previous section (discharge 158434) have been carried out with the M3D-C^1 code [24]. The goal is to provide insight into the plasma response during the application of RMP and NRMP magnetic field perturbations in DIII-D plasmas with conditions similar to those expected in the ITER non-active phase of operations. According to linear ideal [25] and resistive MHD simulations [26][27][28], RMP fields imposed on rational surfaces are expected to be either strongly or weakly screened

depending on the local plasma parameters at each rational surface. Alternatively, under some conditions resistive MHD simulations can result in an amplification of the vacuum RMP field islands [29]. Resistive MHD simulations find that strong screening only occurs on rational surfaces in which the electron perpendicular rotation $\Omega_{\perp e} = \Omega_E + \Omega^*$ is sufficiently far from zero, i.e., $\Omega_{\perp e} = 0 \pm 10$ krad/s [29]. Here, Ω_E is the electron $E \times B$ rotation and Ω^* is the electron diamagnetic rotation. Figure 7 shows the experimentally measured edge $\Omega_{\perp e}$, Ω_E and Ω^* profiles used in the M3D-C[1] simulations of discharge 158434 during the high-power ELMing phase at 2880 ms (dashed lines) and the low-power ELM suppressed phase at 4620 ms (solid lines). Typically, either weak screening or amplification is found in regions with $\Omega_{\perp e} \leq 10$ krad/s [29] shown in figure 7a. Thus, the profiles shown in figures 7ab indicate that strong screening is present on surfaces between ψ_N = 0.92 and 1.0 during the high-power phase and that in the low-power phase this strong screening region is compressed into narrower zone between ψ_N = 0.96 and 1.0. A weak screening region with $\Omega_{\perp e} = 0 \pm 10$ krad/s extends radially inward from the strong screening region to ψ_N = 0.80 during both phases. Figure 8 shows the M3D-C[1] flux surface normal n = 3 components of $B_{m,n=3}$ in G/kA on each rational surface calculated using the output from M3D-C[1] in the SURFMN code [30] between ELMs during the high-power ELMing phase and in the low-power ELM suppressed phase based on the $\Omega_{\perp e}$ profiles shown in figure 7. The vacuum field resonant components are also shown for comparison. Here, m ranges between -8 near ψ_N = 0.84 and -18 at the separatrix. These results show that the screening factors ($B_{m,n=3}^{vacuum}/B_{m,n=3}^{plasma}$) of the m/n = 10/3 and 11/3 islands, on these rational surfaces located just inside the top of the pedestal, reduces $B_{m,n=3}^{vacuum}$ by approximately a factor of 4 in the low-power ELM suppressed phase resulting in island widths that are approximately a factor of 2 smaller as shown in figure 9b. Figure 9a shows the q(ψ_N) profiles at 2880 and 4620 ms along with the positions and widths of the magnetic islands based on data from the M3D-C[1] plasma response simulation shown in figure 8. Note that there are gaps between islands with m < 13 in figure 9a during both the high- and low-power phases of the discharge. This demonstrates the M3D-C[1] plasma response does not result in island overlap (stochasticity) except for a very narrow region outside ψ_N = 0.983 (2880 ms) and ψ_N = 0.989 (4620 ms) as shown in

figure 11. The widths of the vacuum and M3D-C[1] plasma response islands in terms of ψ_N are shown explicitly in figure 9b for reference.

The details of the island widths and positions are of particular interest for testing a hypothesis stating that if a resonant surface or a group of resonant surfaces is excited sufficiently close to the top of the pedestal, tearing-like islands will form and increase the local particle transport [14]. It is then argued that this will cause the density profile to evolve into a peeling-ballooning stable regime where it will remain clamped and result in ELM suppression. This scenario is a variant of an earlier hypothesis in which the width of the pedestal is prevented from expanding inward after an ELM crash by imposing a virtual "wall" which is generated by a region of strong particle transport due to an island or a stochastic layer [31]. In both cases these islands are expected to form as a consequence of a forced tearing mode FTM interaction [32] when a sufficiently strong RMP harmonic is aligned with a rational surface near the top of the pedestal.

As seen in figure 4, the top of the pedestal moves outward in these ^{4}He discharges following the transition from the high-power to the low-power phase. The arrows along the x-axis of figures 8 and 9 show the change in the position of the pedestal top between the two phases. The reduction in the electron pedestal pressure is primarily caused by the elimination of the high-power ^{2}H-NBI heating and a reduction in the pedestal T_e as opposed to a drop in n_e due to the density pump out effect caused by the RMP field observed in ^{2}H discharges. The weak reduction in the pedestal density in the low-power phase compared to that in the high-power phase and the changes in the islands shown in figures 8 and 9 are significantly different than those found in previous two-fluid M3D-C[1] simulations during ^{2}H ELM suppression experiments [14][33]. Figure 10 shows a side-by-side comparison of Poincaré plots, calculated with the TRIP3D field line integration code [34], using results from the linear two-fluid M3D-C[1] simulations shown in figures 8 and 9. The results shown in figures 8, 9 and 10 highlight the changes in the island widths near the top of the pedestal between the high-power (t = 2880 ms) and low-power (t = 4620 ms) phases of the discharge. In the low-power phase the largest island, in close proximity to the top of the pedestal, is m = 11 although the slightly smaller m = 12 island is closer to the top of the pedestal. The m = 10 island is larger than the m = 11 island but

it is well separated from the top of the pedestal, which suggests that it is unlikely be responsible for inhibiting the inward pedestal growth needed to trigger an ELM. In the high-power phase, the largest island (m = 9), is far enough from the top of the pedestal that is not expected to prevent the pedestal from expanding. Based on the island particle transport hypothesis [14], the m = 11 and 12 islands in the low-power phase may induce a change in the particle transport and the small drop in the pedestal density profile seen in figure 4a. This change in the pedestal density profile may be responsible for triggering ELM suppression and preventing the pedestal pressure profile from expanding and crossing the ELM stability boundary. A significant difference in the linear two-fluid M3D-C[1] simulation results between the ^{2}H and ^{4}He experiments is that the islands are weakly amplified in ^{2}H plasmas [14][33] and modestly screened in the ^{4}He plasmas. This suggests that in addition to the three criteria needed for islands to induce a sufficiently large particle transport, *i.e.,* the co-alignment of three locations: (1) the top of the pedestal, (2) the $\Omega_{\perp e} \approx 0$ location and (3) the position of a rational surface associated with a high amplitude poloidal mode number of the applied RMP [14], a threshold in the widths of the islands located near the top of the pedestal or the formation of a stochastic layer near the top of the pedestal caused by island overlap may be a necessary condition.

Figure 11 shows a plot of the fraction of field lines from the M3D-C[1] simulations that hit the divertor originating from thin stochastic layer just inside the unperturbed axisymmetric separatrix, which is referred to as the field line loss fraction. This figure is produced by integrating multiple field lines on each flux surface between $\psi_N = 0.94$ and 1.0 over 200 toroidal turns, approximately 2 km, except when a field line hits a solid surface such as a divertor target plate. The vacuum field line loss fraction for ISS cases in ^{2}H discharges, with RMP coils current of 4 kA, typically covers approximately 15-20% of the outer flux surfaces and has been found to correlate with ELM suppression in some ^{2}H discharges when it exceeds 16.5% [35]. The reduction in the width of field line loss region based on M3D-C[1] simulation results, compared to that of the vacuum field, in these ^{4}He plasmas is significantly different from those in ^{2}H plasmas. While both have a narrow stochastic region near the foot of the pedestal, the difference due to the island amplification in ^{2}H plasmas [14] and island screening in ^{4}He plasmas suggests that a

stochastic layer is formed in the ^{2}H plasmas but not in the ^{4}He plasmas. In addition, the reduction in the pedestal n_e profiles and line average density due to the RMP field seen in ^{2}H plasmas is typically much larger than those in ^{4}He plasmas as shown in figures 2, 3, 4 and 5. This may indicate that the properties of tearing-like islands near the top of the pedestal and the resulting magnetic topology due to the RMP field is significantly different ^{4}He plasmas than in ^{2}H plasmas [15][36] resulting in different particle transport physics. In addition, other mechanism, such as a reduction in the fueling efficiency from recycling, differences in the turbulence or a change in the edge particle pinch and radial electric field [37], may be important to consider in conjunction to the transport resulting from magnetic islands and stochasticity near the top of the pedestal.

A closer examination of figures 9 and 10 at t = 4620 ms reveals three sets of relatively large, closely spaced, islands (m=10-12) near the top of the pedestal along with islands just inside ψ_N = 0.9 that are slightly larger in the high-power than in the low-power phase. Compared to the relatively small islands near the top of the pedestal in the high-power phase, the islands in the low-power phase might be expected to produce more density pump out than is observed experimentally assuming the island transport at the top of the pedestal is correct unless their width is insufficient to induce an increase in the transport as hypothesized above. Based on the change in the density profile shown in figure 4a and the modest reduction in line average density shown in figure 5a, the relatively small drop in density during the low power phase is most likely dominated by the reduced fueling from the ^{2}H-NBI source in the low power phase rather than a change in the transport at the top of the pedestal due to the islands near the top of the pedestal. In ^{2}H plasmas a 15-30% reduction in n_e, due to the RMP field, is typically observed and in some cases the reduction in n_e can be as large as 50% [14]. This does not occur in these ^{4}He plasmas during either the high-power, high-rotation, or low-power, low-rotation, phase. In addition, the conditions during the high-power phase of theses ^{4}He discharges are very similar to those in ^{2}H plasmas where a 4 kA n=3 RMP field reliably triggers density pump out resulting in the evolution of the discharge into an ELM suppressed state, yet the spontaneous evolution of the $\Omega_{\perp e} = 0$ location toward the top of the pedestal does not take place in the high-power phase of these ^{4}He plasmas. It should also be noted that

in both the high- and low-power phase of these ^{4}He discharges τ_E remains constant at approximately 90 ms indicating that there is no change in the thermal transport while the total radiated power drops from 3.6 MW in the high-power phase to 1.3 MW in the low power ECRH phase.

An equally important effect of an externally applied or intrinsic 3D field on the ideal and resistive plasma response is the destabilization of non-resonant modes such as global kink modes and edge kink-peeling modes that can impact the plasma rotation and edge stability [29][38][39]. These modes have been linked to changes in the ELM behavior ranging from mitigation to suppression [40]. These kink-peeling modes are sensitive to the total pressure, the parallel current and to the parallel current gradient in high-β_N H-modes especially as β_N approaches the no wall limit where, in DIII-D, $\beta_N^{no-wall} \approx 2.5\ell_i$. The radial profiles of n = 3, m = -8 through -14 non-resonant edge kink-peeling modes resulting from the M3D-C[1] plasma response simulations at 2880 ms during the high power phase of the discharge are shown in figure 12. Here, β_N =1.96 and the largest kink response, which is due to the m = -14 mode, peaks at $\psi_N \approx 0.97$ with an amplitude of 2.4 G/kA corresponding to approximately 10.1 G with a RMP coil current of 4.2 kA. The large distortion of the edge flux surfaces due to the kink-peeling mode can be seen on the low-field side of the discharge, centered at θ = 0º just outside the $\psi_N \approx 0.9$ surface, in figure 10 with the dashed line at 2880 ms. In the low-power phase with β_N = 0.62 the kink-peeling mode amplitude drops to about 1.2 G/kA or 5.0 G and is strongly compressed into a narrow region at the edge of the plasma as seen in figure 13.

Resistive MHD plasma response modeling with the M3D-C[1] code in the high-power ELMing and low-power ELM suppressed phase of discharge 158434, shown in figure 5, are consistent with M3D-C[1] results when transitioning from ELMing to ELM suppressed regimes in ^{2}H plasmas. Here, a magnetic island forms closer the top of the pedestal in the suppressed phase at 4620 ms than in the ELMing phase as can be seen in figure 8. This change in the island alignment just inside the top of the pedestal is also seen in figure 9 where the m/n = 11/3 and 10/3 islands are amplified in the ELM suppressed phase at 4620 ms relative to the same islands in the ELMing phase at 2880 ms and are positioned closer to the top of the pedestal than the m/n = 9/3 island in the ELMing phase. It is also

noted that these m=9, 10 and 11 islands are completely isolated from edge stochastic region, with its inner boundary located at ψ_N = 0.983 in the high-power phase and at 0.989 in low-power phase. As seen in figure 11, the M3D-C[1] field line loss fraction in the ELM suppressed phase is about 35% larger at ψ_N = 0.995 and somewhat smaller between ψ_N = 0.985 and 0.992 than in the ELMing phase. In ^{2}H plasmas, when transitioning from the ELMing to ELM suppressed state, changes in the magnetic topology that are associated with the plasma response to n = 2 RMP field have been linked to changes in the pedestal density and temperature along with the appearance of stationary n=1 and 2 magnetic structures measured with the DIII-D high-field side magnetic arrays [41]. Although the calculated M3D-C[1] plasma response is similar in these n = 3 ^{4}He discharges, significant changes in the pedestal density are not observed. In addition, the DIII-D high-field side toroidal magnetic arrays see n = 1 and 2 stationary magnetic structures in the high-power ELMing that are approximately a factor of 3 larger in amplitude than in low-power ELM suppressed phase. Here, the high-field side toroidal array sees a 15 G n = 1 b_θ field in the ELMing phase, which is reduced to 4 G in the ELM suppressed phase with no change in the toroidal phase of the mode. A similar change is seen in the n = 2 field. Based on these differences, it is difficult to identify a coherent connection between the calculated M3D-C[1] plasma response and the observed experimental data when comparing transitions from ELMing to ELM suppressed states in n = 2 ^{2}H and n = 3 ^{4}He discharges. This suggests that other parameters must be playing a role in the ELMing to ELM suppressed transition.

5. ELM Suppression in low toroidal rotation NBI heated helium discharges

In discharges similar to 158434, with an initial high power phase of $P_{TOT} = P_{NBI} + P_{ECRH} + P_{OH}$ = 11.7 MW, ELM suppression is obtained during the low-power phase of the discharge using a continuously alternating series of interleaved co- and counter ^{2}H-NBI with P_{NBI} = 1.7 MW. This results in zero net torque with $v_\phi \cong 0$ and $P_{TOT} = P_{NBI} + P_{OH}$ = 3.0 MW, which is slightly above $P_{L\text{-}H}$ in these discharges. An example of the plasma evolution in one of these discharges is shown in figure 14 during discharge 158494 where the line average density increases during the transition from the high- to low-power phase and slowly ramps up during the ELM suppression phase between 2300

and 4000 ms. During the transition from the high-power to low-power H-mode phase, 1800 to 2300 ms in figure 14, a series of low frequency ELM-like events cause large modulations in the electron pedestal density and pressure. These modulations are also seen in the pedestal T_e resulting in ΔW_{ELM} = 6.0 kJ. Here, W_{MHD} drops from 0.9 MJ in the high-power to 0.4 MJ in the low-power phase. The slow increase in the line average electron density is attributed to a influx of high-Z impurities such as FeXXIII (133 nm), NiXVII (249 nm, NiXXVI (165 nm) and MoXXXI (116 nm) into the core plasma between 1880 and 4000 ms. This resulted in a slow increase in the total radiated power from 1.2 MW to 1.8 MW during that period.

As shown in figure 15, at 4000 ms a 6 volt, 15 ms, puff of dichlorodifluoromethane (CC12F2) was injected into the low-field side of the upper DIII-D main chamber causing the total radiated power increase to 2.5 MW for approximately 70 ms and the lower divertor radiated power increased from 65 kW to 1.4 MW. This triggered the H-L back transition seen in the electron density and pedestal pressure (figures 14ab). In this discharge, β_N drops from 1.5 in the high-power H-mode phase to 0.7 in the low-power H-mode phase and to 0.47 in the L-mode phase while β_p drops from 0.55 in the high-power H-mode phase to 0.26 in the low-power H-mode phase and then to 0.18 in the L-mode phase after 4000 ms. The pedestal profiles during the low-power ELM suppressed H-mode phase are typical of those seen during higher power H-mode with a steep gradient region but the height of the pedestal is reduced compared to that in the high-power H-mode phase similar to that shown in figure 4c (158473) at t = 3800 ms during ELM suppression where $\beta_p = 0.22$.

6. ELM behavior in helium discharges with increased heating power and low toroidal rotation

Although ELM suppression was reproducibly obtained in the low-power phase of these discharges using only ECRH or a low-power alternating series of interleaved co- and counter ^{2}H-NBI pulses, when the input power was increased regular ELMs returned. While the ELMs in these discharges with slightly higher co- and counter ^{2}H-NBI pulses appear to be similar in some respects to type-I ELMs seen in ^{2}H plasmas their energy

content normalized to the total stored and pedestal energy is unusually large in some cases and their frequency is found to be inversely proportional to the particle confinement. For example, increasing the average low-power phase $P_{TOT} = P_{NBI} + P_{OH} = 3.0$ MW, used in the ELM suppressed discharges, to $P_{TOT} = P_{NBI} + P_{ECRH} + P_{OH} = 4.3$ MW resulted in the loss of ELM suppression seen in figure 16. Here, the frequency of the diagnostic ^{2}H-NBI pulses was increased compared to that in discharge 158434 (figure 5) while maintaining zero NBI torque with $\Omega_\phi \approx$ -1 krad/s. During the low-power ECRH + ^{2}H-NBI phase of this discharge, starting at 2000 ms, regular ELMs are observed on the lower divertor D_α signals as shown in figure 16b. Although these ELMs appear to be synchronized to the 20 Hz ^{2}H-NBI pulses, a closer look shows that during the time between 2000 and 3500 ms they lead the ^{2}H-NBI pulses and then become fairly well synchronized with the beam pulses between 3400 and 3700 ms. Later in the discharge the ELMs lag the ^{2}H-NBI pulses indicating that they have a slightly higher frequency than the ^{2}H-NBI pulses. In this discharge the ELM frequency during the high-power phase is 75 Hz and the normalized energy loss per ELM is $\Delta W_{ELM}/W_{MHD} = 5.6\%$. During the low-power ECRH + ^{2}H-NBI phase, the normalized energy loss per ELM increases to $\Delta W_{ELM}/W_{MHD} = 11.7\%$ due to a drop in the stored energy (W_{MHD}) from 0.93 MJ to 0.47 MJ, which indicates that the energy loss per ELM is approximately equivalent in both phases although the frequency in the low-power ECRH + ^{2}H-NBI phase is reduced by a factor of 3.75. In addition, during the low-power ECRH + ^{2}H-NBI phase both the line average and pedestal density increase compared to the high-power phase and the lower frequency ELMs cause a significant modulation in the density. Interestingly, $\tau_E = 79$ ms during the high-power phase and increases to 121 ms during the low-power ECRH + ^{2}H-NBI phase while β_N decreases from 1.64 to 0.87 with a normalized pedestal pressure β_p of 0.33. At the same time the pedestal T_e decreases from 0.7 keV to 0.5 keV and Z_{eff}^{brems} increases from 1.7 to 2.1 while $\nu_e^{*,brems}$ increases from 0.52 to 1.3.

In a subsequent discharge, 158495 shown in figure 17, the ^{2}H-NBI pulses used in the low-power phase were replaced by a continuous co-I_p ^{2}H-NBI with $P_{NBI} = 1.7$ MW along with a continuous counter-I_p ^{2}H-NBI with $P_{NBI} = 1.7$ MW and the ECRH was removed in order to maintain an input power and torque similar to that in discharge 158479. This

resulted in an edge Ω_ϕ = -5 krad/s with the central toroidal rotation being Ω_ϕ = 9 krad/s. Here, the line average density increased from 5.44×10^{19} m^{-3} in the high-power phase to 6.16×10^{19} m^{-3} in the lower power ^{2}H-NBI phase. Figure 17 shows a comparison between discharges 158479 and 158495. Discharges 158495 and 158479 both had a total heating power P_{TOT} = 4.3 MW during the low power phase but the ELM frequency f_{ELM} = 35 Hz in 158495 is about 25% higher than in 158479 and the normalized ELM energy loss $\Delta W_{ELM}/W_{MHD} = 7.6\%$ is about 35% smaller. In addition, 158495 has a slightly lower β_N = 0.82 and higher line average density than 158479 while all the other parameters in the low-power, low-rotation, phase are very similar with the exception of the stored energy which increased from 0.48 MJ in 158479 to 0.57 MJ in 158495. The increase in the line average density in 158495 is attributed to the additional ^{2}H-NBI fueling. Typically the ELM frequency decreases with increasing density in ^{2}H RMP mitigated discharges and the normalized ELM energy increases, which is not the case in these two discharges. This suggests that the heating source, *i.e.,* ^{2}H-NBI versus ECRH, may have an impact on the properties of the mitigated ELMs. This hypothesis appears to be consistent with the results shown in figure 18 where the same ^{2}H-NBI and ECRH inputs are used as in 158479 and an increase in the density results in a reduction in f_{ELM} but we need to be cautious about such conclusion since these discharges are operating slightly above the L-H power threshold at very low rotation which can also have an impact on the ELM characteristics.

Figure 18 shows how the ELM frequency changes as a function of the toroidal phase of the applied RMP field and the line average density in discharge 158482. This discharge was a repeat of 158479 with the same heating and plasma parameters but the toroidal phase of the n=3, even parity, RMP field from both the upper and lower coils was rapidly rotated (flipped) by 60º at 3800 ms. This resulted in an increase in the line average density and a reduction in the average f_{ELM} from 28 Hz to 15 Hz as seen in figure 18b. In DIII-D an increase in line average density, indicative of an n = 0 improvement in the particle confinement, is typically observed in ^{2}H plasmas when the toroidal phase of the n = 3 RMP field is flipped from 60º (+4 kA in figure 18a) to 0º (-4 kA in figure 18a) during ELM suppression and ELM mitigation [42][43]. This increase in

the particle confinement in ^{2}H plasmas has been shown to correlate with significant inward shift and narrowing of the E_r profile, a strong increase in the pedestal poloidal ion rotation, a reduction in the edge radial diffusion coefficient and a reduction in the thermal diffusivity across the outer region of the plasma [44]. Since the plasma response to 60º flips in ^{4}He is identical to that seen in ^{2}H plasma, it is assumed that the changes in the pedestal structure are similar in both cases. The working hypothesis is that the n = 3 field mixes constructively or destructively with the intrinsic DIII-D field-errors when the phase is flipped resulting in the observed n = 0 particle confinement change.

Although the ELMs in these ^{4}He discharges have many of the characteristics of type-I ELMs seen in ^{2}H discharges they do not adhere to the usual $\Delta W_{ELM} \propto f_{ELM}^{-1}$ scaling found with type-I ELMs in ^{2}H discharges [45]. In the discharges discussed above, where ELM suppression is not obtained, the distribution of ΔW_{ELM} versus f_{ELM} is shown in figure 19. In these discharges the ELM response to applied n=3, 4 kA, RMP fields is found to be dependent on the injected heating power, the toroidal plasma rotation and the line average density. In the low-power phase of these discharges with P_{NBI} marginally above $P_{L\text{-}H}$ and low toroidal rotation, which is well matched to the conditions expected in ITER during the non-active phase of operations, the ELM behavior is remarkably different than that in the high-power, high toroidal rotation, phase. In the low-power phase, depicted by the dashed 3 MW line in figure 19 of the expected ^{2}H distribution, the ELMs reside in a relatively narrow frequency band. This is rather surprising since the total stored energy (W_{MHD}) during this phase of the discharge ranges between 450 kJ $\leq W_{MHD} \leq$ 635 kJ implying that the average normalized ELM energy $\Delta W_{ELM}/W_{MHD}$ is about 8% and in some cases, such as during last 1000 ms of shot 158482 (figure 18) with W_{MHD}~$500\ kJ$, can exceed 17%. This behavior may be a consequence of operating just above the L-H power threshold at very low toroidal rotation. On the other hand, during the high-power, high v_ϕ, phase of the discharge, with an expected ^{2}H ELM distribution represented by the 12 MW solid line, the ELMs are randomly distributed over a broad range in f_{ELM} and ΔW_{ELM} covering 5 Hz $\leq f_{ELM} \leq$ 190 Hz and 3 kJ $\leq \Delta W_{ELM} \leq$ 85 kJ. This behavior indicates that the ELMs behave differently in both the low-power, low-rotation, and high-power, high-rotation, phases of these ^{4}He discharges with RMP fields

applied compared to the typical distribution of ELMs in high-power, high-rotation, ^{2}H distributions without RMP fields. The differences are especially pronounced during the high-power, high-rotation, phase of the discharge. The underlying causes for these differences are under investigation.

As seen in figure 2 during the high-power, high-rotation, phase of the discharge with $P_{TOT} = P_{NBI} + P_{ECRH} + P_{OH} = 11.6$ MW, the RMP field increases f_{ELM} and reduces ΔW_{ELM} resulting in weak ELM mitigation with $\Delta W_{ELM}/W_{MHD}$ dropping from about 26% to about 19%. In lower-power discharges with $P_{NBI} = 2.3$ MW and $P_{TOT} = P_{NBI} + P_{ECRH} + P_{OH} = 5.7$ MW ELM mitigation, such as that shown in figure 20, the effect of the RMP field is significantly stronger on the density and the ELMs compared to cases with $P_{TOT} = 12.8$ MW and $\beta_p = 0.76$ (*e.g.,* 158434, figure 5) where little or no effect on the density or ELMs is observed. In the lower-power discharge (158411) with $P_{TOT} = 5.7$ MW and $\beta_p = 0.40$, the line average density drops from 5.5×10^{19} m^{-3} without the RMP field to 4.3×10^{19} m^{-3} with the RMP field while $\Delta W_{ELM}/W_{MHD}$ drops from about 17% to about 5%. In this case the ELM frequency increases as the line average and pedestal density decreases similar to that during ELM mitigation in ^{2}H plasmas. These results suggest that there may be a P_{NBI} or β_p threshold in the high-power, high-rotation, phase of these ^{4}He discharges below which strong density pump-out and strong ELM mitigation occurs.

7. Discussion and summary

The primary objective of these experiments was to obtain ELM suppression and/or mitigation in high purity DIII-D ^{4}He plasmas, with low toroidal rotation, near $P_{L\text{-}H}$ in order to match the conditions in ITER during the non-active phase of operations. This was done by starting with a high-power, high toroidal rotation, ^{2}H-NBI heated phase in order to create a stable ELMing reference discharge followed by a low-power phase with approximately zero toroidal rotation. During the high-power phase, with a total heating power $P_{TOT} = 12.8$ MW, the RMP field only had a weak effect on the line average density, the ELM amplitude and f_{ELM} as seen in figure 5 during discharge 158434. Alternatively, when the total heating power was reduced during the high-power phase to $P_{TOT} = 5.7$ MW, such as in discharge 158411 (figure 20), a significant reduction in the line average

density and ELM amplitude was observed during the application of the RMP field and f_{ELM} increased from 18 Hz to 70 Hz similar to RMP ELM mitigation cases in ^{2}H plasmas. As shown in Table 2, both ELM suppression and mitigation were obtained in the low-power phase of these discharges depending on the mix of additional heating power used.

Discharge	Low-power phase	Results
158472	ECRH + 10 Hz ^{2}H beam blips without I_{RMP}	Periodic uncontrolled density increases without ELMs each of which is terminated by large ELMs
158473	ECRH + 10 Hz ^{2}H beam blips with I_{RMP}	Controlled density with short initial ELMing period followed by short ELM suppression
158434	ECRH + 10 Hz ^{2}H beam blips with I_{RMP}	Controlled density with short initial ELMing period followed by long ELM suppression
158494	Continuous balanced co-counter ^{2}H beams with I_{RMP}	Long ELM suppression period followed by H-L back transition triggered by CC12F2 diagnostic puff
158479	ECRH + 20 Hz ^{2}H beam blips with I_{RMP}	ELMs during the entire low-power phase with $f_{ELM} \approx 21$ Hz
158495	Continuous ^{2}H beam with I_{RMP}	ELMs during the entire low-power phase with $f_{ELM} \approx 35$ Hz
158482	ECRH + 20 Hz ^{2}H beam blips, I_{RMP} phase flip	Persistent ELMs in low-power phase. Average f_{ELM} transitions from 28 to 16 Hz after the I_{RMP} phase flip

Table 2 – Summary of ^{4}He ELM mitigation and suppression results during the low-power phase of the discharges discussed in this paper.

Additionally, it was found that ^{4}He discharges operating just above the $P_{L\text{-}H}$ are prone to repetitive, uncontrolled, density and core impurity increases followed by back transitions from the H-mode to an L-mode, similar to ELM-free periods after L-H transitions in ^{2}H plasmas but with several intermittent ELMs during the uncontrolled density rise. The back transitions during the ^{4}He uncontrolled density increases are triggered when high levels of core radiated power, where $P_{rad\text{-}core} \cong P_{L\text{-}H}$, are reached and large ELMs are triggered. In the ITER non-active operating phase, with heating power levels that are marginally above $P_{L\text{-}H}$, these uncontrolled density cycles may be unavoidable and as such could result in a significantly increased risk of disruptions being triggered by loss of plasma control during the fast H-L back transitions, the high levels of radiated power and the interaction of large ELMs with the divertor target plates. In the

experiments discussed here this behavior is a reproducible feature of high-purity ECRH discharges without RMP fields where the total input heating power is marginally above $P_{L\text{-}H}$. Interestingly, with the application of the 4 kA n=3 RMP fields these uncontrolled density cycles are stabilized and the high-Z core impurities are reduced as shown in figure 3 implying that the application of 3-D fields by the ITER control ELM coils may make it possible to avoid this behavior altogether.

In general, the ELM suppressed low-power phase of the ECRH discharges (*e.g.*, 158434, 158473 and 158479) have rather modest levels of high-Z impurities such as Fe, Ni and Mo. On the other hand, discharges with ^{2}H-NBI heating (*e.g.*, 158494) have linearly increasing levels of Fe, Ni and Mo in time that eventually result in a H-L back transition. Additionally, in these ^{2}H-NBI heated discharges, electrons from the accumulation of these high-Z impurities in the core are likely responsible for the linear increase in the line average density, as seen in figure 14, which is not observed in the ECRH discharges. This increase in the high-Z impurities in ^{2}H-NBI heated plasmas has previously been related to a source of metallic impurities in DIII-D due to the interaction of the neutral beams and/or energetic beam ions with unprotected first wall metallic components [18]. On other hand, medium-Z impurity transport studies in ^{2}H-NBI heated ^{4}He plasmas have resulted in essentially an infinite fluorine confinement time in some cases. For example, the back transition seen in figure 14 at 4000 ms was triggered by a 6 volt, 15 ms, puff of dichlorodifluoromethane (CC12F2) injected into the plasma during the ELM suppressed period as shown in figure 15. Alternatively, in ELMing discharge 158479 with ECRH and pulsed ^{2}H-NBI heating (figure 16) the CC12F2 gas puff resulted in a fluorine particle confinement time of 480 ms but did not trigger an H-L back transition. This is about 30% longer than the fluorine particle confinement time in ^{2}H RMP mitigated discharges with a factor of 2 higher ELM frequency and approximately 35% longer than in an ^{2}H NBI heated RMP ELM suppressed DIII-D ^{2}H discharge [46].

Results from these experiments have provided the first clear evidence that long periods of ELM suppression and ELM mitigation can be obtained in ^{4}He plasmas when maintained just above the L-H power threshold with near zero toroidal rotation although the distribution of ELM energies versus frequency in these discharges are quite different

than those in ^{2}H plasmas. These conditions are similar to those expected low-rotation ^{4}He H-mode plasmas during the non-active ITER operational phase. The 3D perturbations fields used to obtain these results are similar to those in ^{2}H plasmas with the I-coil configured for n = 3 even parity using a current of 4.0-4.5 kA.

Acknowledgements

We would like to thank R. Buttery and D. Hill for helpful comments. This work was supported by the US Department of Energy under DE-FC02-04ER54698. DIII-D data shown in this paper can be obtained in digital format by following the links at https://fusion.gat.com/global/D3D_DMP. ITER is the Nuclear Facility INB no. 174. The views and opinions expressed herein do not necessarily reflect those of the ITER Organization.

REFERENCES

[1] T. E. Evans, R. A. Moyer, K. H. Burrell, M. E. Fenstermacher, I. Joseph, A. W. Leonard, T. H. Osborne, G. D. Porter, M. J. Schaffer, P. B. Snyder, P. R. Thomas, J. G. Watkins, and W. P. West, "Edge stability and transport control with resonant magnetic perturbations in collisionless tokamak plasmas," *Nat. Phys.*, vol. 2, no. 6, pp. 419–423, May 2006.

[2] Y. M. Jeon, J.-K. Park, S. W. Yoon, W. H. Ko, S. G. Lee, K. D. Lee, G. S. Yun, Y. U. Nam, W. C. Kim, J.-G. Kwak, K. S. Lee, H. K. Kim, and H. L. Yang, "Suppression of Edge Localized Modes in High-Confinement KSTAR Plasmas by Nonaxisymmetric Magnetic Perturbations," *Phys. Rev. Lett.*, vol. 109, no. 3, pp. 35004-1–4, Jul. 2012.

[3] T. E. Evans, R. A. Moyer, P. R. Thomas, J. G. Watkins, T. H. Osborne, J. A. Boedo, E. J. Doyle, M. E. Fenstermacher, K. H. Finken, R. J. Groebner, M. Groth, J. H. Harris, R. J. La Haye, C. J. Lasnier, S. Masuzaki, N. Ohyabu, D. G. Pretty, T. L. Rhodes, H. Reimerdes, D. L. Rudakov, M. J. Schaffer, G. Wang, and L. Zeng, "Suppression of Large Edge-Localized Modes in High-Confinement DIII-D Plasmas with a Stochastic Magnetic Boundary," *Phys. Rev. Lett.*, vol. 92, no. 23, pp. 235003-1–4, Jun. 2004.

[4] A. Kirk, E. Nardon, R. Akers, M. Bécoulet, G. De Temmerman, B. Dudson, B. Hnat, Y. Q. Liu, R. Martin, P. Tamain, and D. Taylor, "Resonant magnetic perturbation experiments on MAST using external and internal coils for ELM control," *Nucl. Fusion*, vol. 50, no. 3, pp. 34008-1–9, Mar. 2010.

[5] W. Suttrop, T. Eich, J. C. Fuchs, S. Günter, A. Janzer, A. Herrmann, A. Kallenbach, P. T. Lang, T. Lunt, M. Maraschek, R. M. McDermott, A. Mlynek, T.

Pütterich, M. Rott, T. Vierle, E. Wolfrum, Q. Yu, I. Zammuto, and H. Zohm, "First Observation of Edge Localized Modes Mitigation with Resonant and Nonresonant Magnetic Perturbations in ASDEX Upgrade," *Phys. Rev. Lett.*, vol. 106, no. 22, pp. 225004-1–4, Jun. 2011.

[6] Q. Hu, Q. Yu, B. Rao, Y. Ding, X. Hu, and G. Zhuang, "Effect of externally applied resonant magnetic perturbations on resistive tearing modes," *Nucl. Fusion*, vol. 52, no. 8, p. 83011, 2012.

[7] Y. Liang, H. Koslowski, P. R. Thomas, E. Nardon, B. Alper, P. Andrew, Y. Andrew, G. Arnoux, Y. Baranov, M. Bécoulet, M. Beurskens, T. Biewer, M. Bigi, K. Crombe, E. De La Luna, P. de Vries, W. Fundamenski, S. Gerasimov, C. Giroud, M. Gryaznevich, N. Hawkes, S. Hotchin, D. Howell, S. Jachmich, V. Kiptily, L. Moreira, V. Parail, S. Pinches, E. Rachlew, and O. Zimmermann, "Active Control of Type-I Edge-Localized Modes with n=1 Perturbation Fields in the JET Tokamak," *Phys. Rev. Lett.*, vol. 98, no. 26, pp. 265004-1–4, Jun. 2007.

[8] S. A. Sabbagh, J. W. Berkery, R. E. Bell, J. M. Bialek, S. P. Gerhardt, J. E. Menard, R. Betti, D. A. Gates, B. Hu, O. N. Katsuro-Hopkins, B. P. LeBlanc, F. M. Levinton, J. Manickam, K. Tritz, and H. Yuh, "Advances in global MHD mode stabilization research on NSTX," *Nucl. Fusion*, vol. 50, no. 2, pp. 25020-1–9, Feb. 2010.

[9] P. T. Lang, A. Loarte, G. Saibene, L. R. Baylor, M. Becoulet, M. Cavinato, S. Clement-Lorenzo, E. Daly, T. E. Evans, M. E. Fenstermacher, Y. Gribov, L. D. Horton, C. Lowry, Y. Martin, O. Neubauer, N. Oyama, M. J. Schaffer, D. Stork, W. Suttrop, P. Thomas, M. Tran, H. R. Wilson, A. Kavin, and O. Schmitz, "ELM control strategies and tools: status and potential for ITER," *Nucl. Fusion*, vol. 53, no. 4, pp. 43004-1–24, Apr. 2013.

[10] A. Loarte, G. Huijsmans, S. Futatani, L. R. Baylor, T. E. Evans, D. M. Orlov, O. Schmitz, M. Becoulet, P. Cahyna, Y. Gribov, A. Kavin, A. Sashala Naik, D. J. Campbell, T. Casper, E. Daly, H. Frerichs, A. Kischner, R. Laengner, S. Lisgo, R. A. Pitts, G. Saibene, and A. Wingen, "Progress on the application of ELM control schemes to ITER scenarios from the non-active phase to DT operation," *Nucl. Fusion*, vol. 54, no. 3, pp. 33007-1–18, Mar. 2014.

[11] L. R. Baylor, N. Commaux, T. C. Jernigan, S. J. Meitner, S. K. Combs, R. C. Isler, E. A. Unterberg, N. H. Brooks, T. E. Evans, A. W. Leonard, T. H. Osborne, P. P. B., P. B. Snyder, E. J. Strait, M. E. Fenstermacher, C. J. Lasnier, R. A. Moyer, A. Loarte, G. T. A. Huijsmans, and S. Futatani, "Reduction of edge localized mode intensity on DIII-D by on-demand triggering with high frequency pellet injection and implications for ITER," *Phys. Plasmas*, vol. 20, p. 82513, 2013.

[12] D. Campbell, "Challenges in Bruning Plasma Physics: the ITER Research Plan," in *24th IAEA Fusion Energy Conference*, 2012, p. ITR/P1-18.

[13] P. Gohil, T. E. Evans, M. E. Fenstermacher, J. R. Ferron, T. H. Osborne, J. M. Park, O. Schmitz, J. T. Scoville, and E. A. Unterberg, "L–H transition studies on DIII-D to determine H-mode access for operational scenarios in ITER," *Nucl. Fusion*, vol. 51, no. 10, pp. 103020-1–9, Oct. 2011.

[14] M. R. Wade, R. Nazikian, J. S. DeGrassie, T. E. Evans, N. M. Ferraro, R. A. Moyer, D. M. Orlov, R. J. Buttery, M. E. Fenstermacher, A. M. Garofalo, M. A. Lanctot, G. R. McKee, T. H. Osborne, M. A. Shafer, W. M. Solomon, P. B. Snyder, W. Suttrop, A. Wingen, E. A. Unterberg, and L. Zeng, "Advances in the physics understanding of ELM suppression using resonant magnetic perturbations in DIII-D," *Nucl. Fusion*, vol. 55, no. 2, pp. 23002-1–18, Feb. 2015.

[15] T. E. Evans, M. E. Fenstermacher, R. A. Moyer, T. H. Osborne, J. G. Watkins, P. Gohil, I. Joseph, M. J. Schaffer, L. R. Baylor, M. Bécoulet, J. A. Boedo, K. H. Burrell, J. S. DeGrassie, K. H. Finken, T. Jernigan, M. W. Jakubowski, C. J. Lasnier, M. Lehnen, A. W. Leonard, J. Lonnroth, E. Nardon, V. Parail, O. Schmitz, B. Unterberg, and W. P. West, "RMP ELM suppression in DIII-D plasmas with ITER similar shapes and collisionalities," *Nucl. Fusion*, vol. 48, no. 2, pp. 24002-1–10, Feb. 2008.

[16] G. L. Jackson, P. M. Anderson, J. Bialek, W. P. Cary, G. L. Campbell, A. M. Garofalo, R. Hatcher, A. G. Kellman, R. J. La Haye, A. Nagy, G. A. Navratil, M. Okabayashi, C. J. Pawley, H. Reimerdes, J. T. Scoville, E. J. Strait, and D. D. Szymanski, "Initial Results from the New Internal Magnetic Field Coils for Resistive Wall Mode Stabilization in the DIII-D Tokamak," in *30th EPS Conference on Controlled Fusion and Plasma Physics, St. Petersburg, 7-11 July 2003, vol. 27A, part 4*, 2003, vol. 27, no. July, p. 4.47-4.50.

[17] E. A. Unterberg, O. Schmitz, T. E. Evans, R. Maingi, N. H. Brooks, M. E. Fenstermacher, S. Mordijck, R. A. Moyer, and D. M. Orlov, "The effects of an open and closed divertor on particle exhaust during edge-localized mode suppression by resonant magnetic perturbations in DIII-D," *Nucl. Fusion*, vol. 50, no. 3, pp. 34011-1–9, Mar. 2010.

[18] M. A. Van Zeeland, N. M. Ferraro, W. W. Heidbrink, G. J. Kramer, D. C. Pace, X. Chen, T. E. Evans, R. K. Fisher, M. García-Muñoz, J. M. Hanson, M. J. Lanctot, L. L. Lao, R. A. Moyer, R. Nazikian, and D. M. Orlov, "Modulation of prompt fast-ion loss by applied n = 2 fields in the DIII-D tokamak," *Plasma Phys. Control. Fusion*, vol. 56, no. 1, p. 15009, Jan. 2014.

[19] O. Sauter, C. Angioni, and Y. R. Lin-Liu, "Neoclassical conductivity and bootstrap current formulas for general axisymmetric equilibria and arbitrary collisionality regime," *Phys. Plasmas*, vol. 6, no. 7, pp. 2834–2839, 1999.

[20] R. J. Hawryluk, "Physics of Plasmas Close to Thermonuclear Conditions," in *Commission of the European Communities, International School of Plasmas Physics (Pergamon Press, 1981)*, 1981, pp. 19–46.

[21] T. W. Petrie, T. E. Evans, N. H. Brooks, M. E. Fenstermacher, J. R. Ferron, C. T. Holcomb, B. Hudson, A. W. Hyatt, T. C. Luce, C. J. Lasnier, S. Mordijck, R. A. Moyer, T. H. Osborne, P. A. Politzer, M. E. Rensink, M. J. Schaffer, P. B. Snyder, and J. G. Watkins, "Results from radiating divertor experiments with RMP ELM suppression and mitigation," *Nucl. Fusion*, vol. 51, no. 7, pp. 73003-1–10, Jul. 2011.

[22] T. E. Evans, R. A. Moyer, J. G. Watkins, P. R. Thomas, T. H. Osborne, J. A. Boedo, M. E. Fenstermacher, K. H. Finken, R. J. Groebner, M. Groth, J. Harris, G.

L. Jackson, R. J. La Haye, C. . J. Lasnier, M. . J. Schaffer, G. Wang, and L. Zeng, "Suppression of large edge localized modes in high confinement DIII-D plasmas with a stochastic magnetic boundary," *J. Nucl. Mater.*, vol. 337–339, pp. 691–696, Mar. 2005.

[23] R. A. Moyer, T. E. Evans, T. H. Osborne, P. R. Thomas, M. Becoulet, J. Harris, K. H. Finken, J. A. Boedo, E. J. Doyle, M. E. Fenstermacher, P. Gohil, R. J. Groebner, M. Groth, G. L. Jackson, R. J. La Haye, C. J. Lasnier, A. W. Leonard, G. R. McKee, H. Reimerdes, T. L. Rhodes, D. L. Rudakov, M. J. Schaffer, P. B. Snyder, M. R. Wade, G. Wang, J. G. Watkins, W. P. West, and L. Zeng, "Edge localized mode control with an edge resonant magnetic perturbation," *Phys. Plasmas*, vol. 12, no. 5, pp. 56119-1–11, 2005.

[24] N. M. Ferraro, "Calculations of two-fluid linear response to non-axisymmetric fields in tokamaks," *Phys. Plasmas*, vol. 19, no. 5, pp. 56105-1–9, 2012.

[25] J.-K. Park, A. H. Boozer, J. E. Menard, S. P. Gerhardt, and S. A. Sabbagh, "Shielding of external magnetic perturbations by torque in rotating tokamak plasmas," *Phys. Plasmas*, vol. 16, no. 8, pp. 82512-1–7, 2009.

[26] M. S. Chu, L. L. Lao, M. J. Schaffer, T. E. Evans, E. J. Strait, Y. Q. Liu, M. J. Lanctot, H. Reimerdes, Y. Liu, T. A. Casper, and Y. Gribov, "Response of a resistive and rotating tokamak to external magnetic perturbations below the Alfvén frequency," *Nucl. Fusion*, vol. 51, no. 7, pp. 73036-1–10, Jul. 2011.

[27] M. Becoulet, F. Orain, P. Maget, N. Mellet, X. Garbet, E. Nardon, G. T. A. Huysmans, T. Casper, A. Loarte, P. Cahyna, A. Smolyakov, F. L. Waelbroeck, M. Schaffer, T. Evans, Y. Liang, O. Schmitz, M. Beurskens, V. Rozhansky, and E. Kaveeva, "Screening of resonant magnetic perturbations by flows in tokamaks," *Nucl. Fusion*, vol. 52, no. 5, pp. 54003-1–16, May 2012.

[28] Y. Liu, A. Kirk, and E. Nardon, "Full toroidal plasma response to externally applied nonaxisymmetric magnetic fields," *Phys. Plasmas*, vol. 17, no. 12, pp. 122502-1–17, 2010.

[29] N. M. Ferraro, T. E. Evans, L. L. Lao, R. A. Moyer, R. Nazikian, D. M. Orlov, M. W. Shafer, E. A. Unterberg, M. R. Wade, and A. Wingen, "Role of plasma response in displacements of the tokamak edge due to applied non-axisymmetric fields," *Nucl. Fusion*, vol. 53, no. 7, pp. 73042-1–8, Jul. 2013.

[30] M. J. Schaffer, J. E. Menard, M. P. Aldan, J. M. Bialek, T. E. Evans, and R. A. Moyer, "Study of in-vessel nonaxisymmetric ELM suppression coil concepts for ITER," *Nucl. Fusion*, vol. 48, no. 2, pp. 24004-1–14, Feb. 2008.

[31] P. B. Snyder, T. H. Osborne, K. H. Burrell, R. J. Groebner, A. W. Leonard, R. Nazikian, D. M. Orlov, O. Schmitz, M. R. Wade, and H. R. Wilson, "The EPED pedestal model and edge localized mode-suppressed regimes: Studies of quiescent H-mode and development of a model for edge localized mode suppression via resonant magnetic perturbations," *Phys. Plasmas*, vol. 19, no. 5, 2012.

[32] T. S. Hahm and R. M. Kulsrud, "Forced magnetic reconnection," *Phys. Fluids*, vol. 28, no. 8, p. 2412, 1985.

[33] D. M. Orlov, R. A. Moyer, T. E. Evans, C. Paz-Soldan, N. M. Ferraro, R. Nazikian, J. S. deGrassie, B. A. Grierson, D. Eldon, M. E. Fenstermacher, J. D. King, N. C. Logan, M. J. Lanctot, R. Maingi, P. B. Snyder, E. J. Strait, and A. Wingen, "Suppression of type-I ELMs with reduced RMP coil set on DIII-D," *Nucl. Fusion*, vol. 56, no. 3, p. 36020, 2016.

[34] T. E. Evans, R. A. Moyer, and P. Monat, "Modeling of stochastic magnetic flux loss from the edge of a poloidally diverted tokamak," *Phys. Plasmas*, vol. 9, no. 12, pp. 4957–4967, 2002.

[35] M. E. Fenstermacher, T. E. Evans, T. H. Osborne, M. J. Schaffer, M. P. Aldan, J. S. DeGrassie, P. Gohil, I. Joseph, R. a. Moyer, P. B. Snyder, R. J. Groebner, M. Jakubowski, a. W. Leonard, and O. Schmitz, "Effect of island overlap on edge localized mode suppression by resonant magnetic perturbations in DIII-D," *Phys. Plasmas*, vol. 15, no. 5, p. 56122, 2008.

[36] T. E. Evans, K. H. Burrell, M. E. Fenstermacher, R. A. Moyer, T. H. Osborne, M. J. Schaffer, W. P. West, L. W. Yan, J. A. Boedo, E. J. Doyle, G. L. Jackson, I. Joseph, C. J. Lasnier, A. W. Leonard, T. L. Rhodes, P. R. Thomas, J. G. Watkins, and L. Zeng, "The physics of edge resonant magnetic perturbations in hot tokamak plasmas," *Phys. Plasmas*, vol. 13, no. 5, pp. 56121-1–11, 2006.

[37] W. M. Stacey and T. E. Evans, "The role of radial particle pinches in ELM suppression by resonant magnetic perturbations," *Nucl. Fusion*, vol. 51, no. 1, pp. 13007-1–6, Jan. 2011.

[38] M. J. Lanctot, H. Reimerdes, A. M. Garofalo, M. S. Chu, J. M. Hanson, Y. Q. Liu, G. A. Navratil, I. N. Bogatu, Y. In, G. L. Jackson, R. J. La Haye, M. Okayabashi, J. K. Park, M. J. Schaffer, O. Schmitz, E. J. Strait, and A. D. Turnbull, "Measurement and modeling of three-dimensional equilibria in DIII-D," *Phys. Plasmas*, vol. 18, no. 5, 2011.

[39] G. T. A. Huysmans, "External kink (peeling) modes in x-point geometry," *Plasma Phys. Control. Fusion*, vol. 47, no. 12, pp. 2107–2121, 2005.

[40] A. Wingen, N. M. Ferraro, M. W. Shafer, E. A. Unterberg, T. E. Evans, D. L. Hillis, and P. B. Snyder, "Impact of plasma response on plasma displacements in DIII-D during application of external 3D perturbations," *Nucl. Fusion*, vol. 54, no. 6, pp. 64007-1–11, Jun. 2014.

[41] R. Nazikian, C. Paz-Soldan, J. D. Callen, J. S. deGrassie, D. Eldon, T. E. Evans, N. M. Ferraro, B. a Grierson, R. J. Groebner, S. R. Haskey, C. C. Hegna, J. D. King, N. C. Logan, G. R. Mckee, R. a Moyer, M. Okabayashi, D. M. Orlov, T. H. Osborne, J. Park, T. L. Rhodes, M. W. Shafer, P. B. Snyder, W. M. Solomon, E. J. Strait, and M. R. Wade, "Pedestal Bifurcation and Resonant Field Penetration at the Threshold of Edge-Localized Mode Suppression in the DIII-D Tokamak," *Phys. Rev. Lett.*, vol. 105002, no. March, pp. 1–5, 2015.

[42] T. E. Evans, "ELM mitigation techniques," *J. Nucl. Mater.*, vol. 438, pp. S11–S18, Jul. 2013.

[43] T. E. Evans, "Resonant magnetic perturbations of edge-plasmas in toroidal confinement devices," *Plasma Phys. Control. Fusion*, vol. 57, no. 12, p. 123001,

2015.

[44] T. M. Wilks, W. M. Stacey, and T. E. Evans, "Analysis of toroidal phasing of resonant magnetic perturbation effects on edge transport in the DIII-D tokamak," *Phys. Plasmas*, vol. 20, no. 5, 2013.

[45] A. Herrmann, "Overview on stationary and transient divertor heat loads," *Plasma Phys. Control. Fusion*, vol. 44, pp. 897–917, 2002.

[46] B. A. Grierson, K. H. Burrell, R. M. Nazikian, W. M. Solomon, A. M. Garofalo, E. A. Belli, G. M. Staebler, M. E. Fenstermacher, G. R. McKee, T. E. Evans, D. M. Orlov, S. P. Smith, C. Chrobak, and C. Chrystal, "Impurity confinement and transport in high confinement regimes without edge localized modes on DIII-D," *Phys. Plasmas*, vol. 22, no. 5, 2015.

Figure captions:

Figure 1 – ITER Similar Shape (ISS) used in DIII-D ^{4}He ELM suppression/mitigation experiments showing the location of the upper and lower I-coil (RMP coil), the ECRH deposition region, the locations of the ECE diagnostic channels and the lower divertor fs01-04 filterscope views.

Figure 2 –Evolution of discharge 158472 showing: a) the line average density, pedestal density and lower divertor D_α recycling, b) the ^{2}H neutral beam power (P_{NBI}), ECRH power (P_{ECRH}) and I-(RMP) coil current (I_{RMP}) and c) the FeXXIII (133 nm) line radiation measured in the core plasmas using the SPRED dual range EUV survey spectrometer diagnostic system.

Figure 3 – Evolution of discharge 158473 showing: a) the line average density, pedestal density and lower divertor D_α recycling, b) the ^{2}H neutral beam power (P_{NBI}), ECRH power (P_{ECRH}) and I-(RMP) coil current (I_{RMP}) and c) the FeXXIII (133 nm) line radiation measured in the core plasmas using the SPRED dual range EUV survey spectrometer diagnostic system.

Figure 4 – Profile changes in discharge 158473 during the high-power phase (t = 2555 ms) and the low-power phase with ELMs (t = 3500 ms) and without ELMs (t = 3800 ms) showing: a) the electron density, b) the electron temperature, c) the electron pressure and d) the electron pressure gradient.

Figure 5 – Evolution of discharge 158434 showing: a) the line average density and lower divertor D_α recycling, b) the ^{2}H neutral beam power (P_{NBI}) and ECRH power (P_{ECRH}), and c) the pedestal toroidal rotation v_ϕ and I-(RMP) coil current (I_{RMP}).

Figure 6 – a) Profiles of the edge toroidal rotation (Ω_ϕ) and b) radial electric field (E_r) during the high-power ELMing phase at t = 2800 ms (black) and low-power ECRH ELM suppressed phase at t = 4620 ms (red).

Figure 7 – a) An expanded view of the edge $\Omega_{\perp e}$ profile during the high-power ELMing phase at t = 2800 ms and the low-power ECRH ELM suppressed phase at t = 4750 ms in discharge 158434 and b) edge profiles showing Ω_E, Ω^* and $\Omega_{\perp e}$ during both the high- and low-power phases of the discharge.

Figure 8 – Radial distribution of the applied δb_r^{vac} vacuum n = 3 resonant magnetic field components and corresponding plasma response δb_r^{plasma} from M3D-C[1] simulations using the profile data shown in figure 7 as a function of normalized poloidal flux.

Figure 9 – a) q(ψ_N) profiles during the high-power ELMing phase (2880 ms) and the low-power ELM suppressed phase (4620 ms) showing the positions and widths of the islands based on δb_r^{plasma} from M3D-C[1] simulations shown in figure 8 and b) island vacuum widths (dashed lines) compared to M3D-C[1] island widths (solid lines) in ψ_N at 2880 and 4620 ms.

Figure 10 – Poincaré plots showing the magnetic field line structure, from the M3D-C[1] simulations shown in figure 8, due to resonant islands, non-resonant kink modes and edge stochasticity as a function of poloidal angle and normalized poloidal flux during the (left) high-power phase at 2880 ms and (right) the low-power phase at 4820 ms. The thick dashed lines show the approximate extent of the strong M3D-C[1] kink response based on the data shown in figures 12 and 13.

Figure 11 – The fraction of field lines from the edge stochastic region, based on the M3D-C[1] simulations shown in figure 8, that strike the lower divertor as a function or the normalized poloidal flux (ψ_N) for each time shown in the Poincaré plots in figure 10.

Figure 12 – Radial distribution of n = 3, m = -8 through -14 non-resonant plasma response fields calculated with the two-fluid resistive MHD code M3D-C[1] during the high-power phase of discharge 158434.

Figure 13 – Radial distribution of n = 3, m = -8 through -14 non-resonant plasma response fields calculated with the two-fluid resistive MHD code M3D-C[1] during the low-power phase of discharge 158434.

Figure 14 – Evolution of a) the line average density, pedestal density, I- (RMP) coil current and lower divertor D_α signal near the inner strikepoint along with b) the electron pedestal pressure and c) the balanced co- and counter- ^{2}H neutral beam power (P_{NBI}) as well as the ECRH power (P_{ECRH}) during the high-power ELMing and low-power ELM suppressed phases in discharge 158494.

Figure 15 – Evolution of the total radiated power and lower divertor radiated power following a CC12F2 (dichlorodifluoromethane) diagnostic impurity gas puff at 4000 ms in discharge 158494 that triggered an H-L back transition.

Figure 16 – Evolution of a) the total input power (P_{TOT}), line average density, pedestal density, I- (RMP) coil current and initial ^{4}He gas injection along with b) the lower divertor D_α signal near the inner strikepoint, ^{2}H neutral beam power (P_{NBI}) and the ECRH power (P_{ECRH}) during the high-power ELMing and low-power ELMing phases in discharge 158479.

Figure 17 – Comparison of a) the line average density and I- (RMP) coil current, bc) the lower divertor D_α signal near the inner strikepoint, d) the plasma stored energy (W_{MHD}), e) the ^2H neutral beam power (P_{NBI}) and f) the ECRH power (P_{ECRH}) during the high-power ELMing and low-power ELM suppressed phases in discharges 158479 and 158495.

Figure 18 – Evolution of a) the line average density, pedestal density and the lower divertor D_α signal near the inner strikepoint during a 60º toroidal phase flip of the n = 3 I- (RMP) coil current along with b) the distribution of ELM energies and frequencies for each I- (RMP) coil configuration shown in a) during the low-power phase of discharge 158482 using the same ^2H neutral beam power (P_{NBI}) and ECRH power (P_{ECRH}) configuration as in discharge 158479 (figure 14b).

Figure 19 – Distribution of ELM energies versus frequency based on changes in the fast diamagnetic stored plasma energy signal during ELMs observed in each of the discharges analyzed. Different symbols are used for each discharge. The discharge numbers associated with each symbol are listed above the figure.

Figure 20– Evolution of a) the total input power (P_{TOT}), line average density, pedestal density, I- (RMP) coil current and initial ^4He gas injection along with b) the lower divertor D_α signal near the inner strikepoint, ^2H neutral beam power (P_{NBI}) and the ECRH power (P_{ECRH}) during the high-power ELMing and ELM mitigated phases in discharge 158411.

ITER Similar Shape 158488.2860

Helium with P_{ECRH} = 3.0 MW

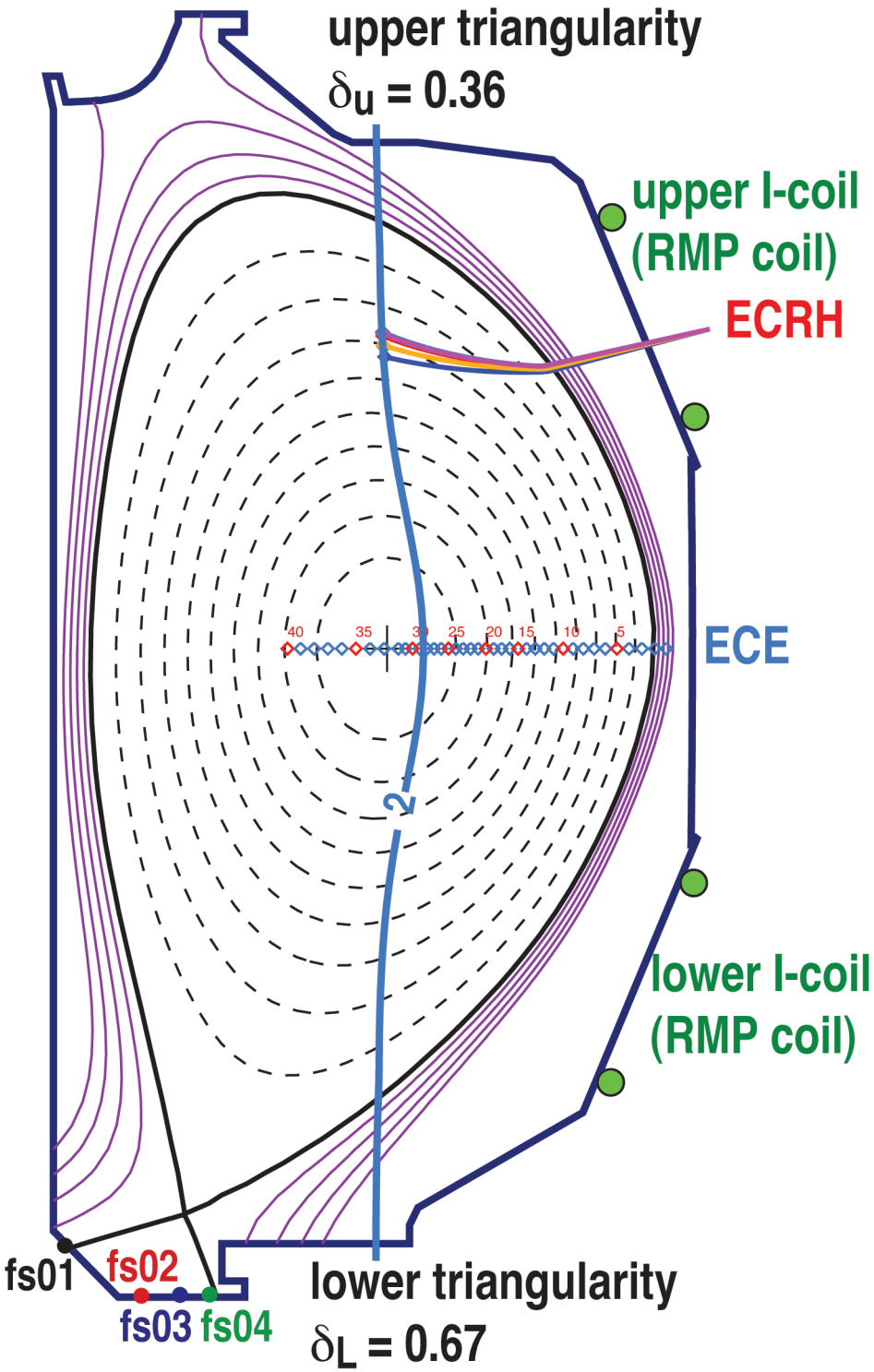

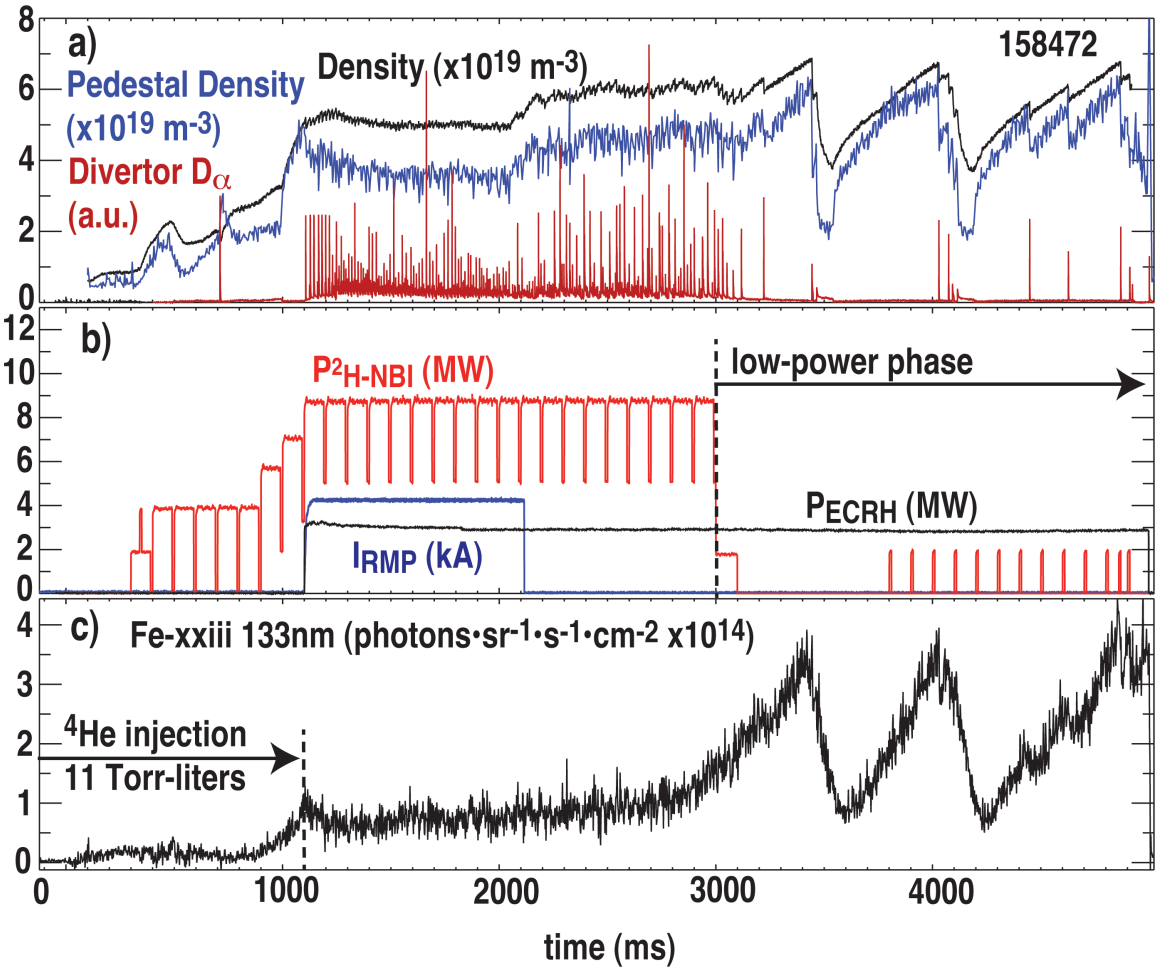

Evans Figure 2

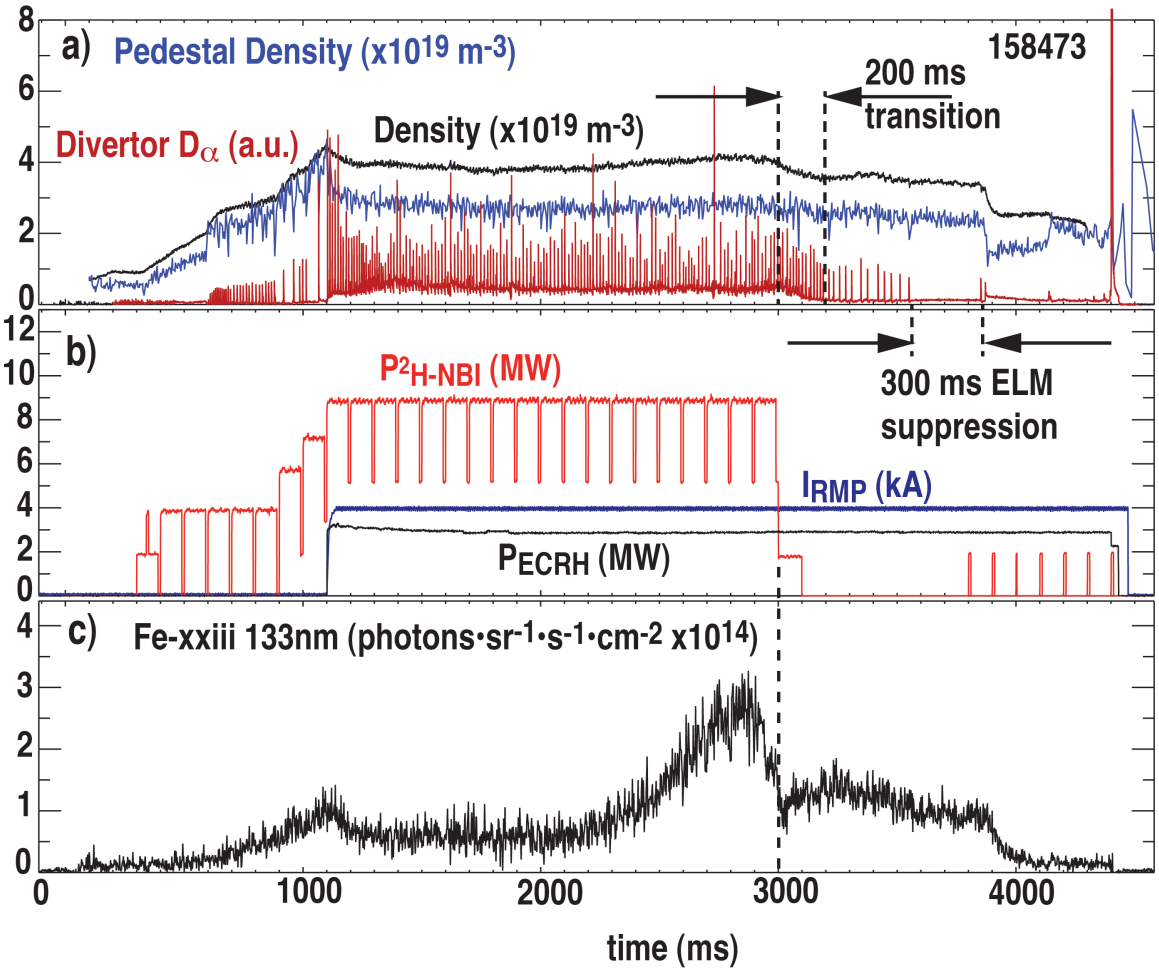

Evans Figure 3

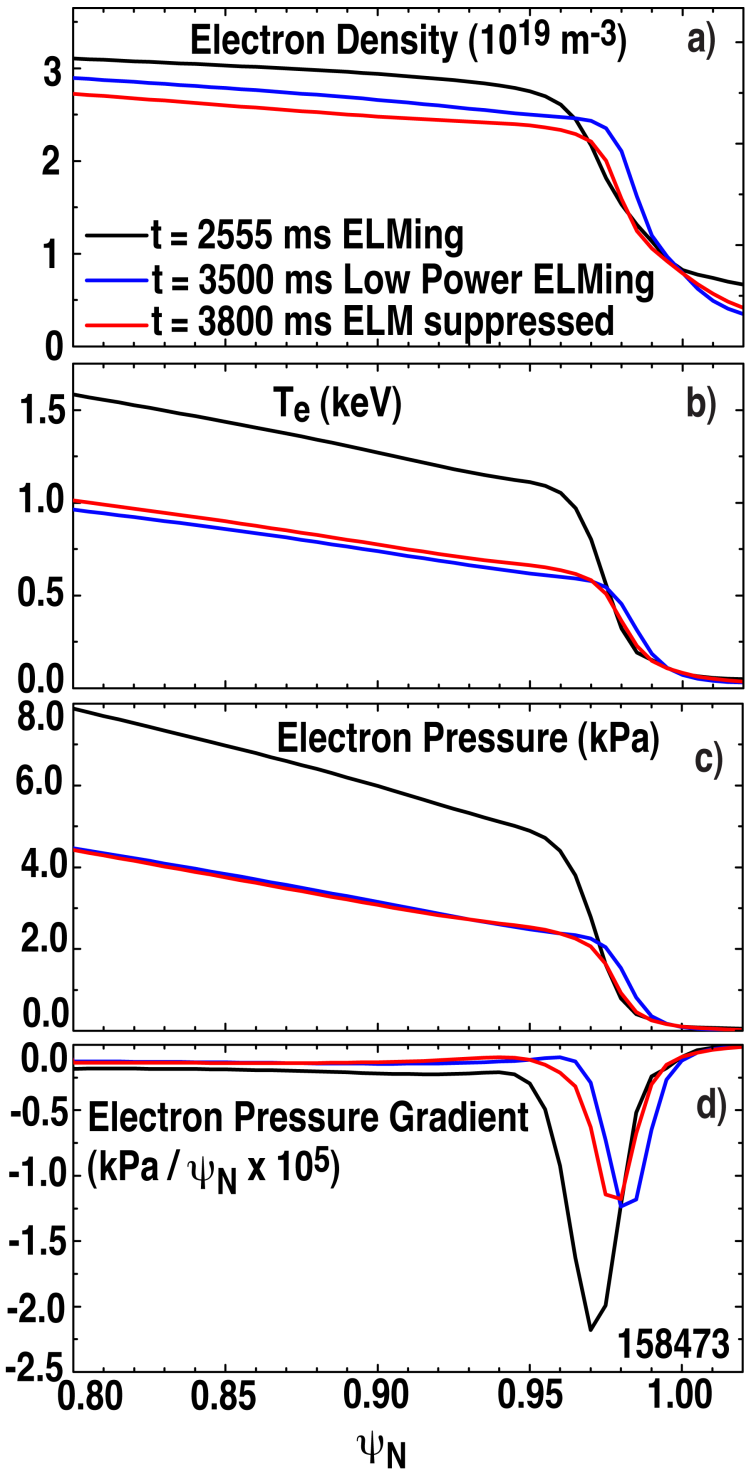

Evans Figure 4

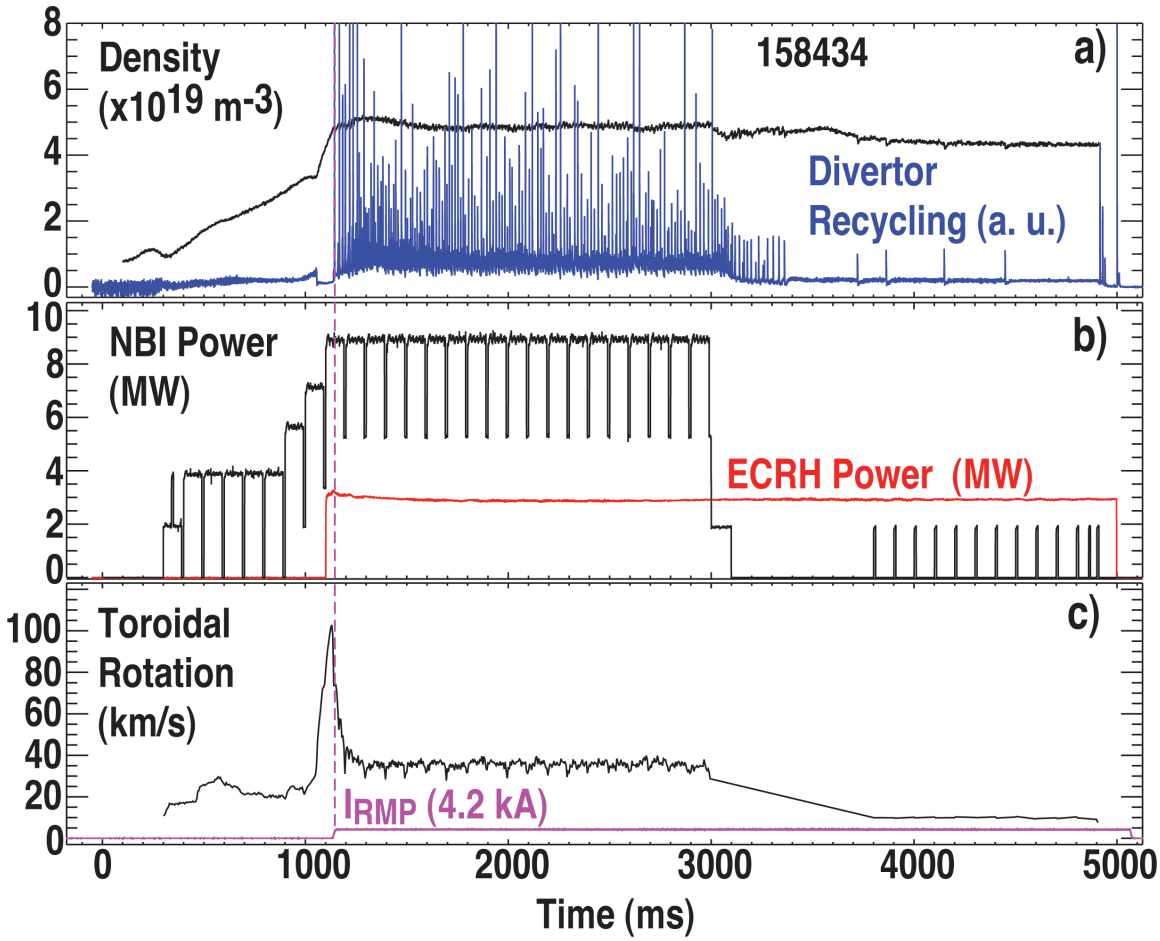

Evans Figure 5

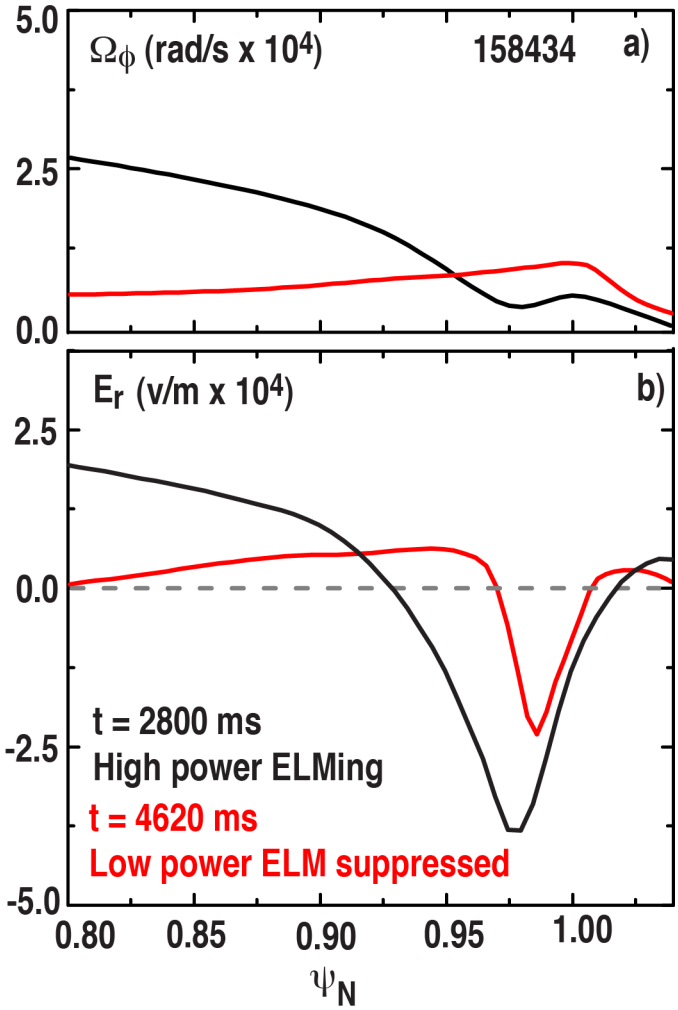

Evans Figure 6

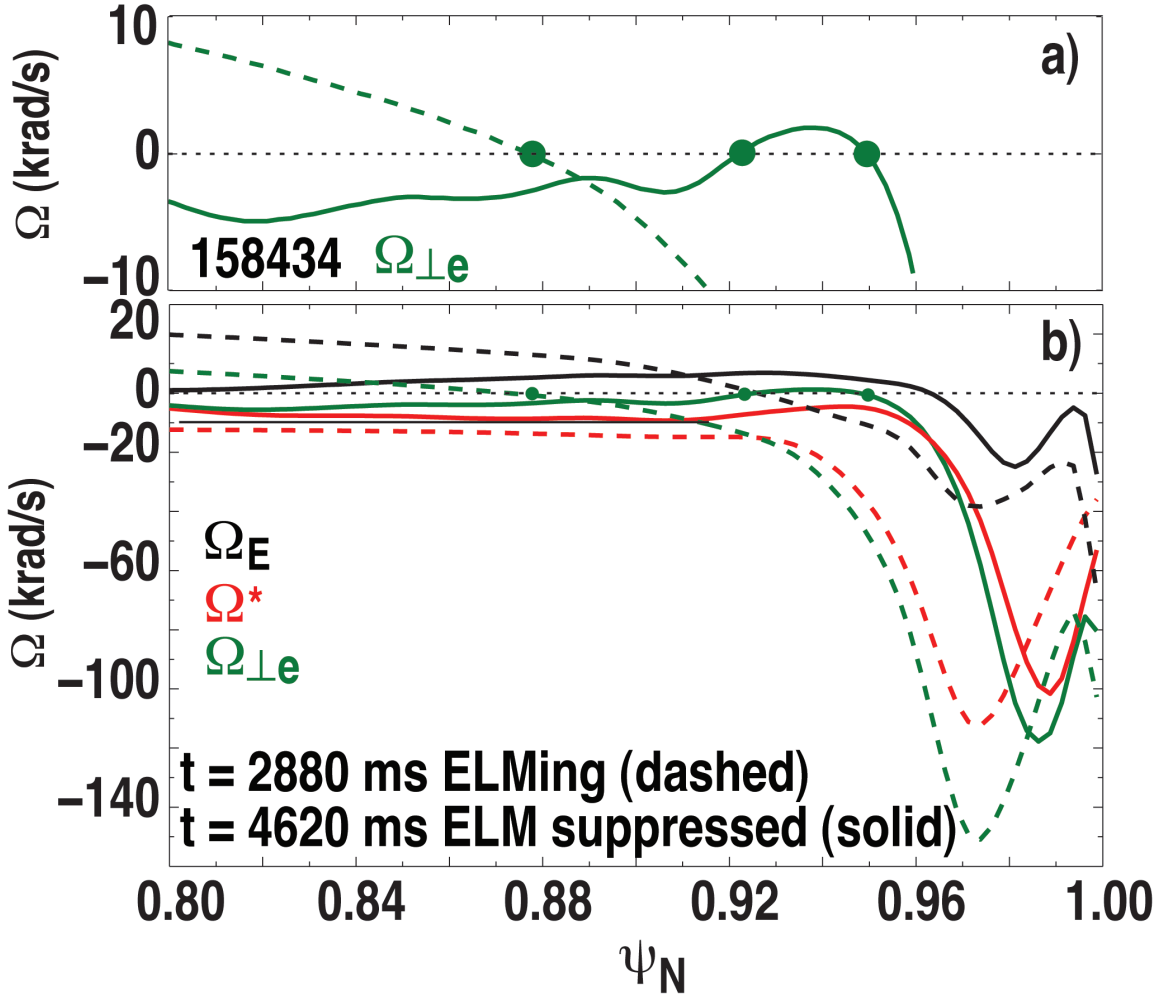

Evans Figure 7

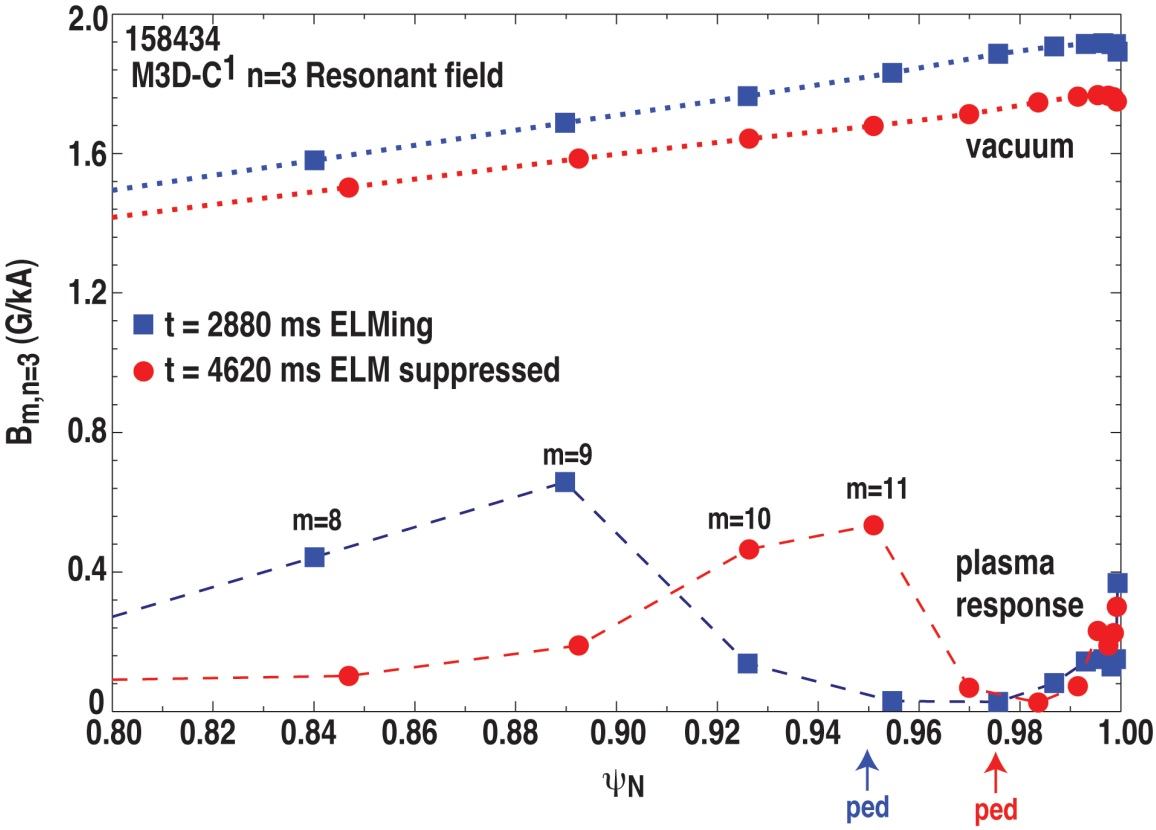

Evans Figure 8

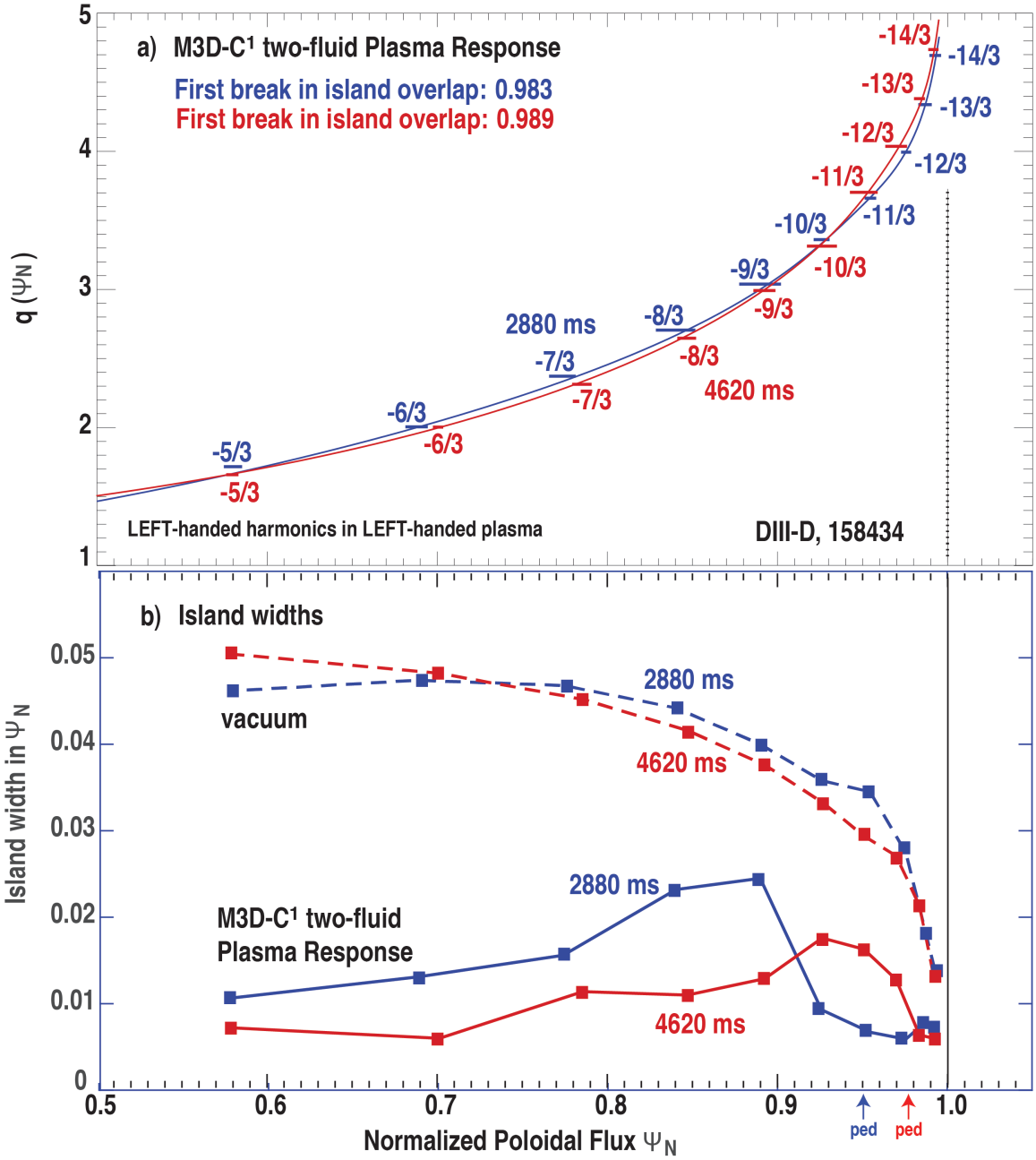

Evans Figure 9

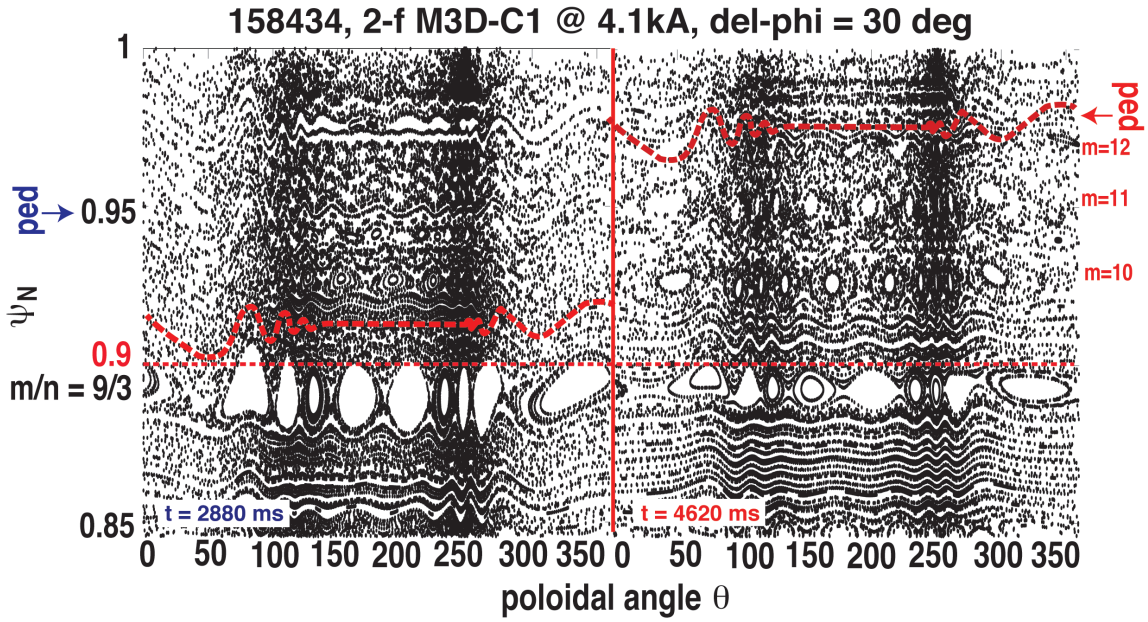

Evans Figure 10

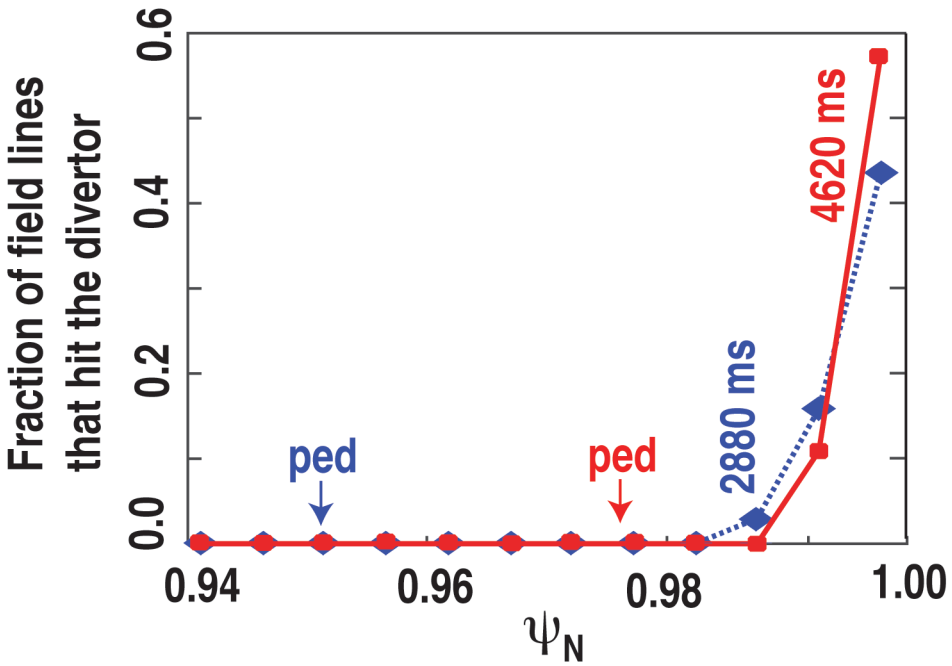

Evans Figure 11

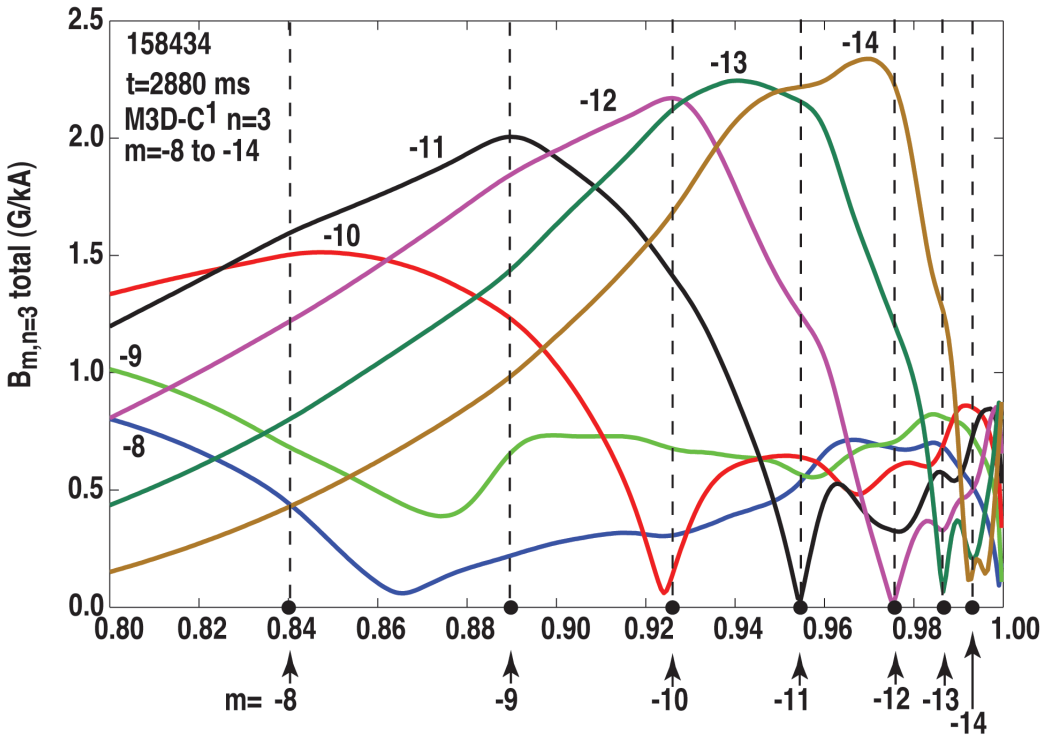

Evans Figure 12

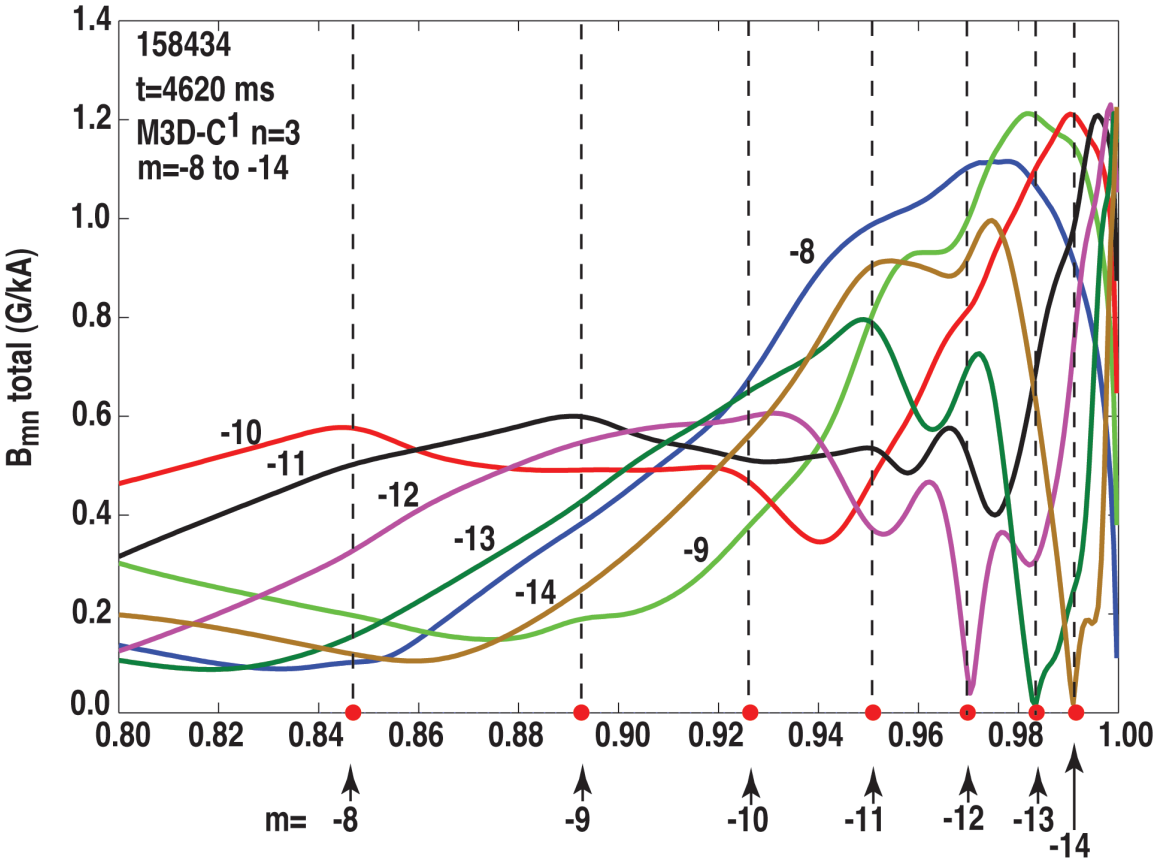

Evans Figure 13

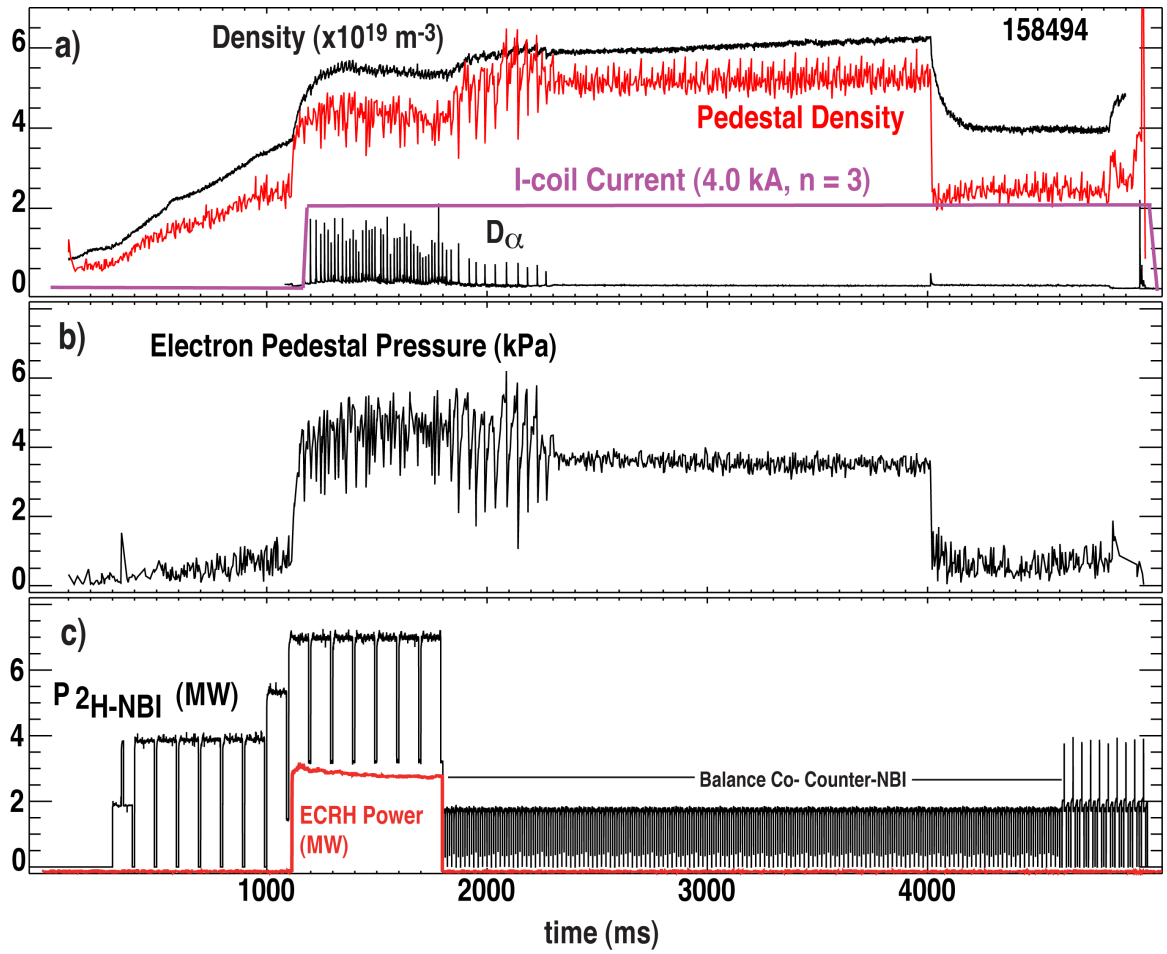

Evans Figure 14

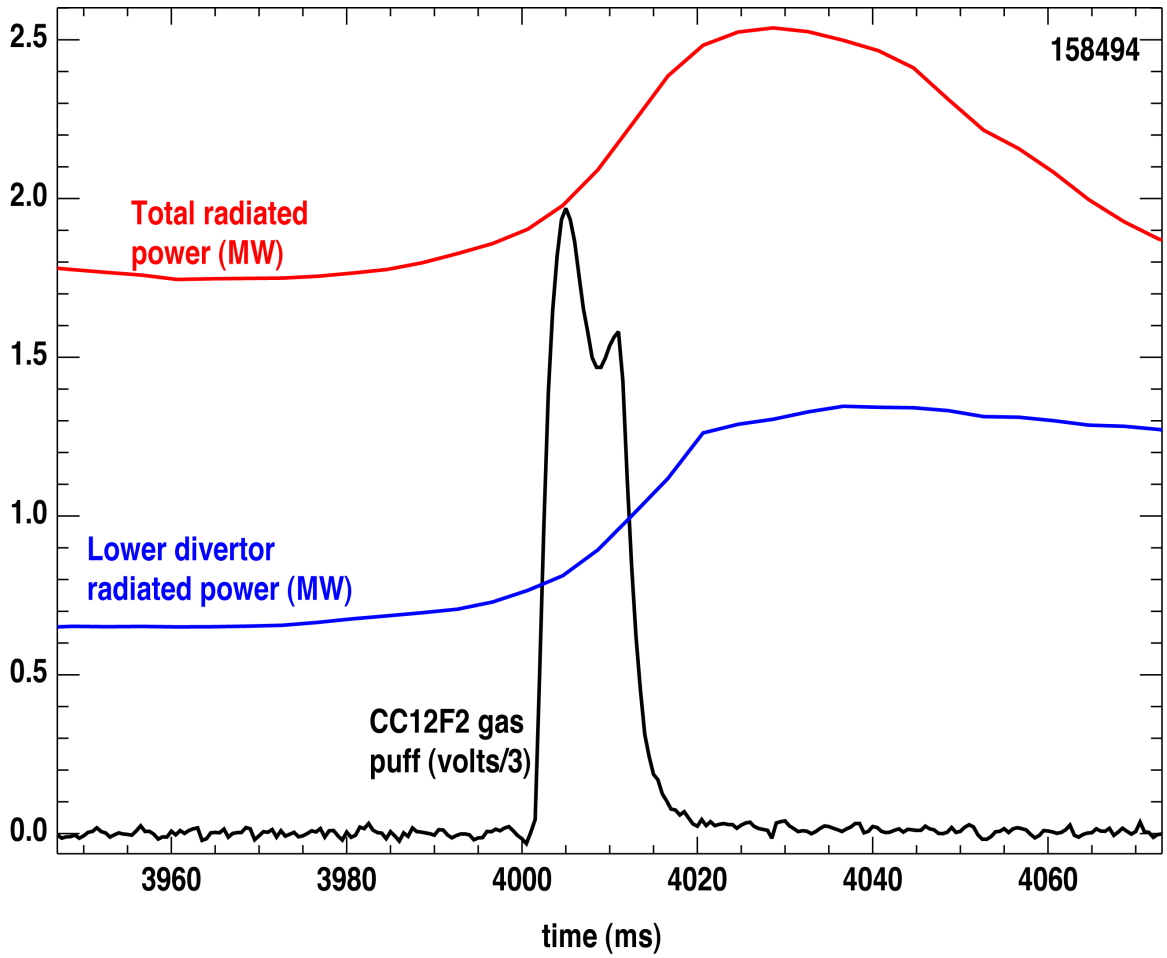

Evans Figure 15

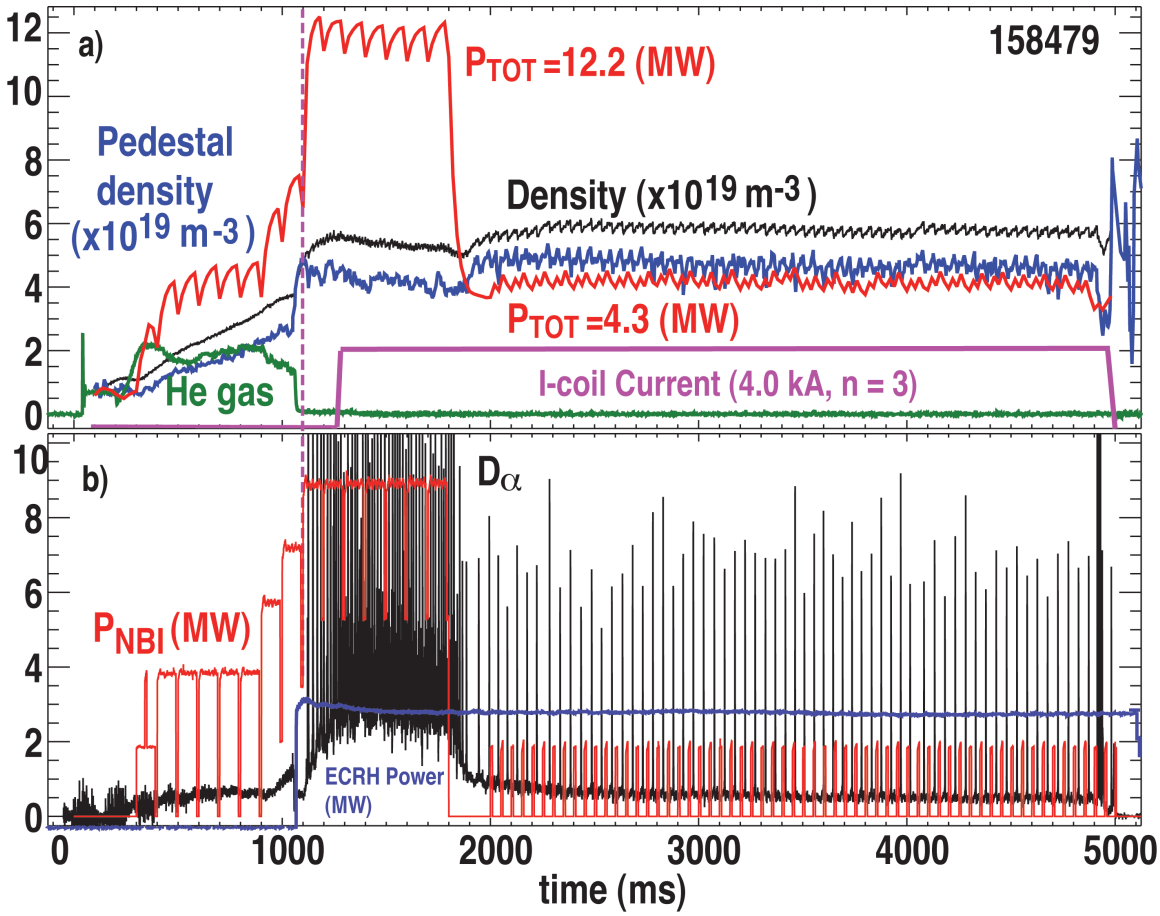

Evans Figure 16

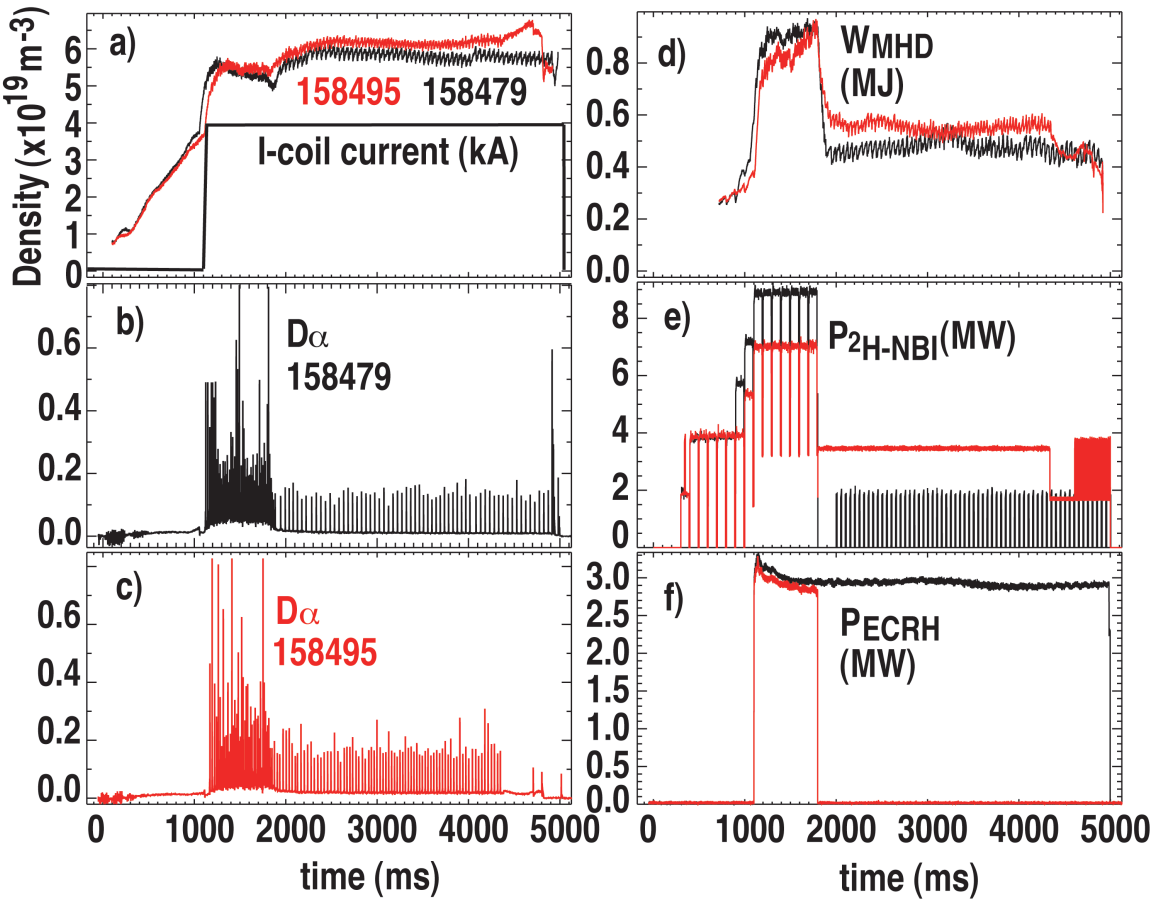

Evans Figure 17

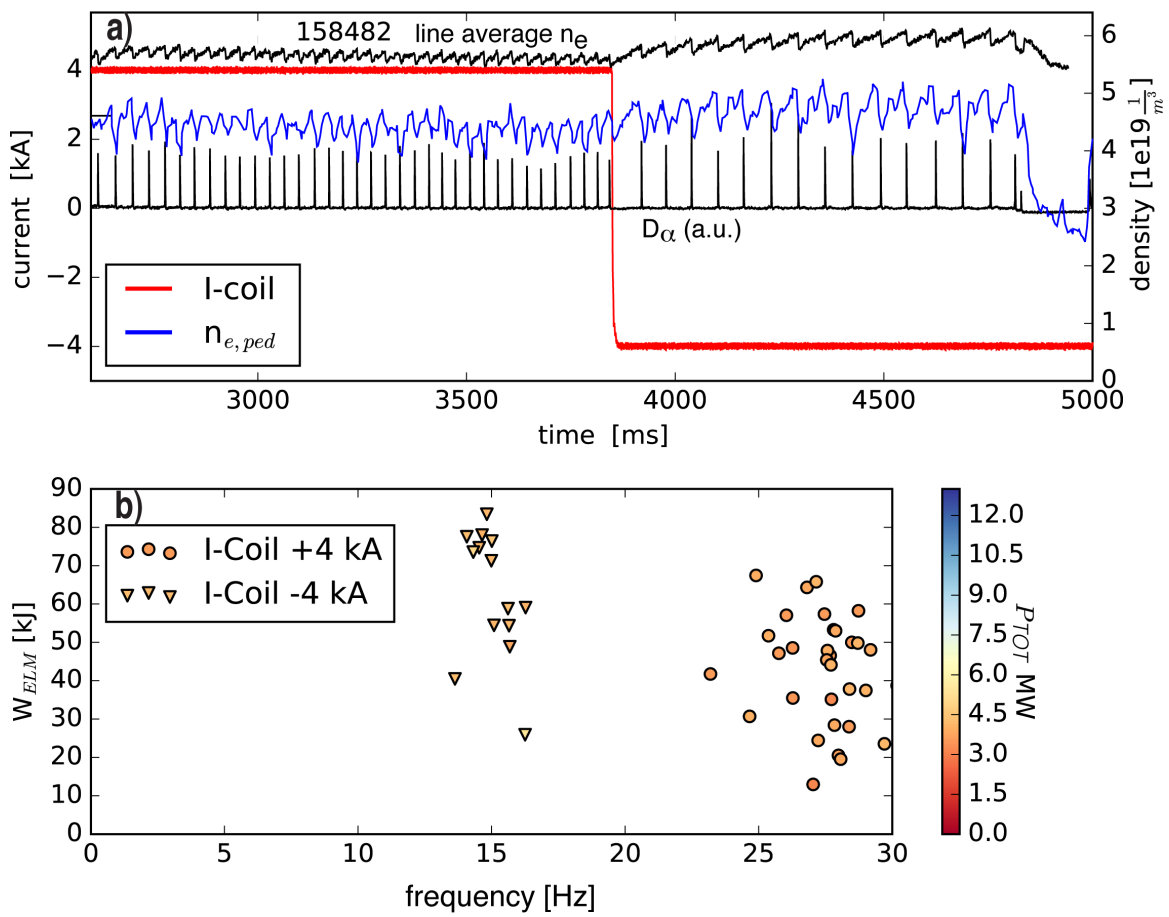

Evans Figure 18

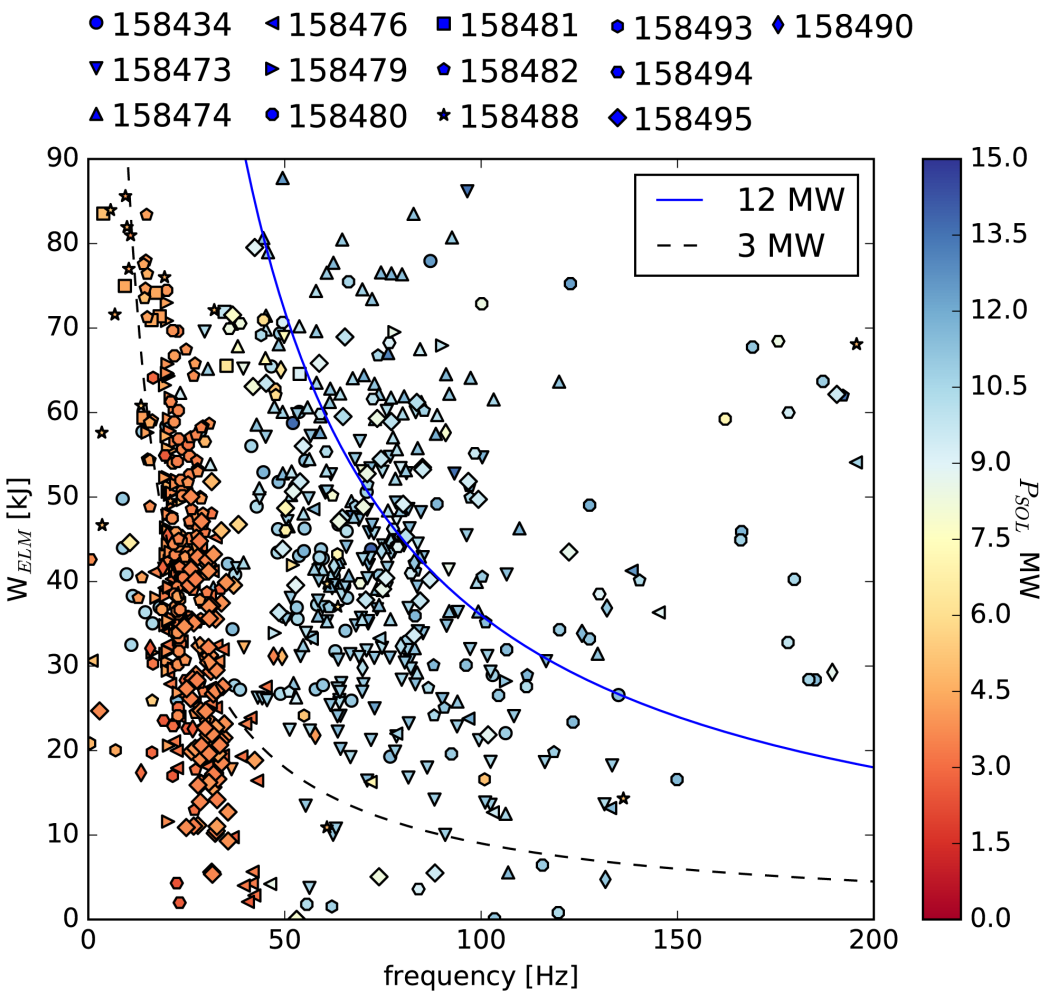

Evans Figure 19

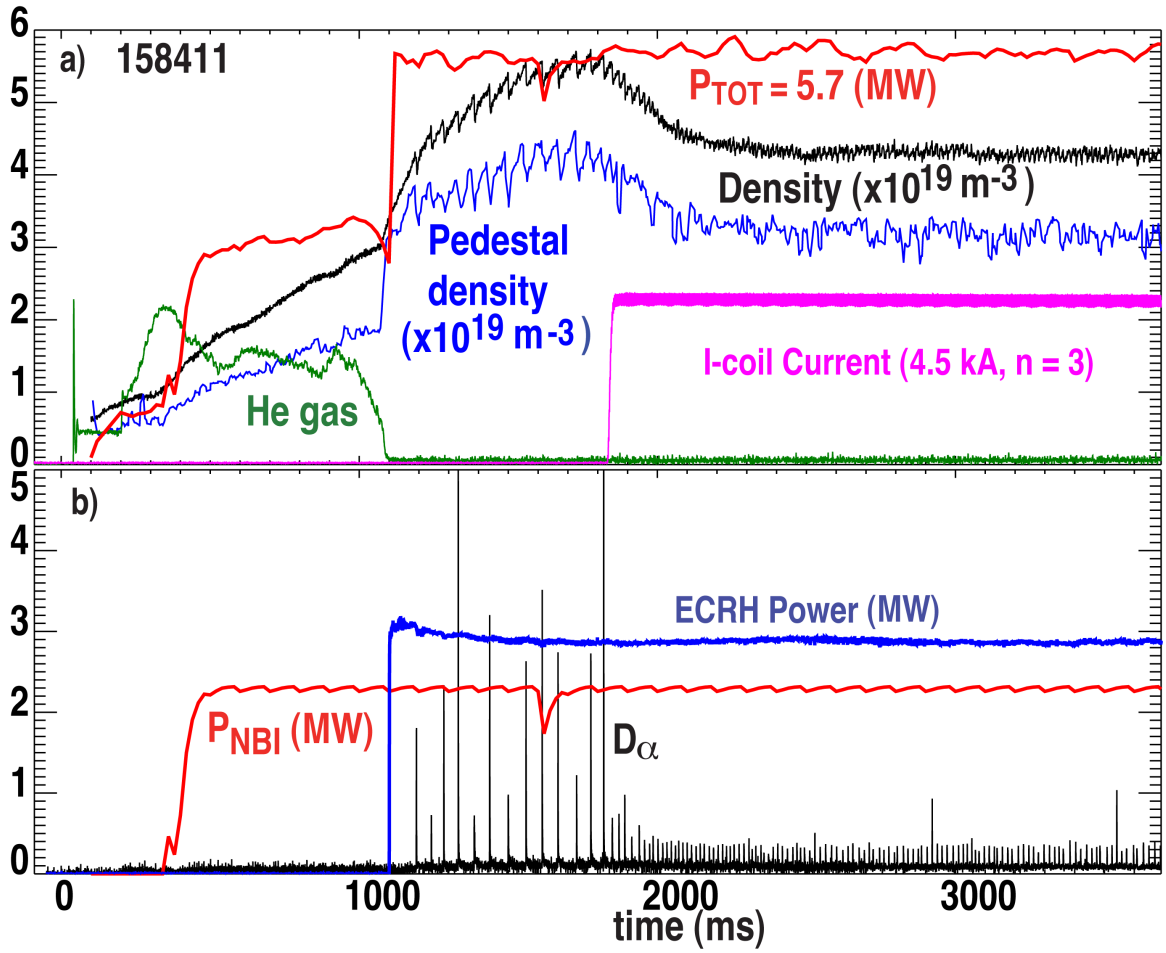

Evans Figure 20